The Astrophysical Journal, 948:5 (20pp), 2023 May 1 https://doi.org/10.3847/1538-4357/acbfb7

The SDSS-V Black Hole Mapper Reverberation Mapping Project: Unusual Broad-line Variability in a Luminous Quasar

Logan B. Fries[1], Jonathan R. Trump[1], Megan C. Davis[1], C. J. Grier[2,3], Yue Shen[4,5], Scott F. Anderson[6], Tom Dwelly[7], Michael Eracleous[8], Y. Homayouni[8], Keith Horne[9], Mirko Krumpe[10], Sean Morrison[4], Jessie C. Runnoe[11], Benny Trakhtenbrot[12], Roberto J. Assef[13], W. N. Brandt[14,15,16], Joel Brownstein[17], Collin Dabbieri[11], Alexander Fix[18], Gloria Fonseca Alvarez[1,19], Sara Frederick[11], P. B. Hall[20], Anton M. Koekemoer[21], Jennifer I-Hsiu Li[22], Xin Liu[4,5], Mary Loli Martínez-Aldama[23,24], Claudio Ricci[13,25], Donald P. Schneider[8], Hugh W. Sharp[1], Matthew J. Temple[13], Qian Yang[4,26], Grisha Zeltyn[12], and Dmitry Bizyaev[27,28]

[1] Department of Physics, 196A Auditorium Road, Unit 3046, University of Connecticut, Storrs, CT 06269, USA
[2] Steward Observatory, The University of Arizona, 933 North Cherry Avenue, Tucson, AZ 85721, USA
[3] Department of Astronomy, University of Wisconsin-Madison, Madison, WI 53706, USA
[4] Department of Astronomy, University of Illinois at Urbana-Champaign, Urbana, IL 61801, USA
[5] National Center for Supercomputing Applications, University of Illinois at Urbana-Champaign, Urbana, IL 61801, USA
[6] Astronomy Department, University of Washington, Box 351580, Seattle, WA 98195, USA
[7] Max-Planck-Institut für extraterrestrische Physik, Giessenbachstraße, D-85748 Garching, Germany
[8] Department of Astronomy & Astrophysics and Institute for Gravitation and the Cosmos, The Pennsylvania State University, 525 Davey Lab, University Park, PA 16802, USA
[9] SUPA Physics and Astronomy, University of St. Andrews, Fife KY16 9SS, UK
[10] Leibniz-Institut für Astrophysik (AIP), An der Sternwarte 16, 14482 Potsdam, Germany
[11] Department of Physics and Astronomy, Vanderbilt University, Nashville, TN 37235, USA
[12] School of Physics and Astronomy, Tel Aviv University, Tel Aviv 69978, Israel
[13] Instituto de Estudios Astrofísicos, Facultad de Ingeniería y Ciencias, Universidad Diego Portales, Av. Ejército Libertador 441, Santiago, Chile
[14] Department of Astronomy & Astrophysics, 525 Davey Lab, The Pennsylvania State University, University Park, PA 16802, USA
[15] Institute for Gravitation and the Cosmos, The Pennsylvania State University, University Park, PA 16802, USA
[16] Department of Physics, 104 Davey Lab, The Pennsylvania State University, University Park, PA 16802, USA
[17] Department of Physics and Astronomy, University of Utah, 115 S. 1400 E., Salt Lake City, UT 84112, USA
[18] Department of Astrophysical & Planetary Sciences, University of Colorado, 2000 Colorado Avenue, Boulder, CO 80309, USA
[19] NSF's National Optical-Infrared Astronomy Research Laboratory, 950 N. Cherry Avenue, Tucson, AZ 85719, USA
[20] Department of Physics and Astronomy, York University, Toronto, ON M3J 1P3, Canada
[21] Space Telescope Science Institute, 3700 San Martin Drive, Baltimore, MD 21218, USA
[22] Department of Astronomy, University of Michigan, Ann Arbor, MI 48109, USA
[23] Instituto de Física y Astronomía, Facultad de Ciencias, Universidad de Valparaíso, Gran Bretaña 1111, Valparaíso, Chile
[24] Departamento de Astronomía, Universidad de Chile, Casilla 36D, Santiago, Chile
[25] Kavli Institute for Astronomy and Astrophysics, Peking University, Beijing 100871, People's Republic of China
[26] Center for Astrophysics | Harvard & Smithsonian, 60 Garden Street, Cambridge, MA 02138, USA
[27] Apache Point Observatory and New Mexico State University, P.O. Box 59, Sunspot, NM, 88349-0059, USA
[28] Sternberg Astronomical Institute, Moscow State University, Moscow, Russia
Received 2022 November 30; revised 2023 February 24; accepted 2023 February 24; published 2023 April 27

Abstract

We present a high-cadence multiepoch analysis of dramatic variability of three broad emission lines (Mg II, Hβ, and Hα) in the spectra of the luminous quasar ($\lambda L_\lambda(5100\,\text{Å}) = 4.7 \times 10^{44}$ erg s^{-1}) SDSS J141041.25+531849.0 at $z = 0.359$ with 127 spectroscopic epochs over nine years of monitoring (2013–2022). We observe anticorrelations between the broad emission-line widths and flux in all three emission lines, indicating that all three broad emission lines "breathe" in response to stochastic continuum variations. We also observe dramatic radial velocity shifts in all three broad emission lines, ranging from $\Delta v \sim 400$ km s^{-1} to $\sim$800 km s^{-1}, that vary over the course of the monitoring period. Our preferred explanation for the broad-line variability is complex kinematics in the gas in the broad-line region. We suggest a model for the broad-line variability that includes a combination of gas inflow with a radial gradient, an azimuthal asymmetry (e.g., a hot spot), superimposed on the stochastic flux-driven changes to the optimal emission region ("line breathing"). Similar instances of line-profile variability due to complex gas kinematics around quasars are likely to represent an important source of false positives in radial velocity searches for binary black holes, which typically lack the kind of high-cadence data we analyze here. The long-duration, wide-field, and many-epoch spectroscopic monitoring of SDSS-V BHM-RM provides an excellent opportunity for identifying and characterizing broad emission-line variability, and the inferred nature of the inner gas environment, of luminous quasars.

Unified Astronomy Thesaurus concepts: Active galactic nuclei (16); Quasars (1319); Supermassive black holes (1663)

Supporting material: animations

1. Introduction

Active galactic nuclei (AGNs) are powered by supermassive black holes (SMBHs) that are actively accreting matter at the centers of massive galaxies (Lynden-Bell 1969). A hallmark signature of many AGNs is the existence of broad emission lines, as first described by Seyfert (1943). Such lines arise from photoionization of the gas of the broad-line region (BLR), which is a distribution of gas that is thought to be moving in virialized orbits (Bentz et al. 2009; Shapovalova 2010; Barth et al. 2011a, 2011b; Grier et al. 2013) close to the central black hole. As the radius of the BLR is of the order of light-days, it is difficult to spatially resolve with current technology. To date, there have been only a handful of studies that have been able to spatially resolve the BLR using near-infrared interferometry (Gravity Collaboration et al. 2020). Investigating the structure of the BLR generally requires indirect techniques such as reverberation mapping (Blandford & McKee 1982; Peterson 1993; Cackett et al. 2021).

Reverberation mapping (RM) is a technique that utilizes the fact that variations in the continuum flux of the AGN are followed by variations in the broad emission lines from the BLR, with a time delay, τ, that corresponds to the light-travel time between the continuum-emitting region and the BLR. The time delay is thus related to the typical radius of the BLR by the relation $R_{\rm BLR} = c\tau$. If we assume that the BLR is virialized, then the mass of the central black hole is determined by the virial product, namely,

$$M_{\rm RM} = f\frac{v^2 R_{\rm BLR}}{G} \quad (1)$$

where v is the velocity of the BLR gas, $R_{\rm BLR}$ is the BLR radius, and G is the gravitational constant. A dimensionless factor f is introduced into the equation to parameterize the inclination angle, unknown geometry, and orientation of the BLR. The dimensionless factor f is calibrated by comparison with spatially resolved BLR measurements (Sturm et al. 2018), the kinematics of stars and gas near the AGN (e.g., Grier et al. 2013; Woo et al. 2015), and/or velocity-resolved reverberation mapping (e.g., Pancoast et al. 2014; Grier et al. 2017a).

Both observations (Wilhite et al. 2006; Park et al. 2012; Barth et al. 2015; Dexter et al. 2019; Homan et al. 2020; Wang et al. 2020) and photoionization modeling (Korista & Goad 2004; Cackett & Horne 2006; Goad & Korista 2014) have demonstrated that an increase in central flux from the AGN accretion disk results in an increase in the radius of the BLR "optimal emitting region" and a corresponding decrease in the orbital velocity of the gas since the line emission originates further out. This phenomenon is known as "line breathing" and manifests itself as an anticorrelation between the broad-line flux and width of the BLR over time. Quantifying the breathing behaviors of broad emission lines provides valuable constraints on the geometry, kinematics, and photoionzation of the BLR (Wang et al. 2020).

The continuum flux of quasars exhibits variability of order $\sim$10% on timescales of weeks to years that is thought to be driven by thermal fluctuations in the accretion disk (Ulrich et al. 1997; Vanden Berk et al. 2004; Kelly et al. 2009; MacLeod et al. 2010). Periodicity in quasar photometric light curves has been a popular method for searching for SMBH binary candidates (Valtonen et al. 2008; Ackermann et al. 2015; Graham et al. 2015; Li et al. 2016, 2019; Charisi et al. 2016; Sandrinelli et al. 2018; Severgnini et al. 2018; Chen et al. 2020; Liao et al. 2021; Zhang 2022). However, Vaughan et al. (2016) demonstrated that the stochastic variability of single (nonbinary) quasars can resemble a periodic signal that can span a few periods, leading to false-positive identification of SMBH binaries. An alternative method for identifying binary SMBHs is to search for periodic radial velocity shifts in broad emission lines (Gaskell 1983; Loeb 2010; Eracleous et al. 2012; Shen et al. 2013; Liu et al. 2014; Runnoe et al. 2017; Guo et al. 2019) akin to spectroscopic binary stars. This method requires high-cadence, long-term spectroscopic monitoring because the binary orbits have periods of the order of decades (Yu 2002).

Radial velocity shifts of broad emission lines can also result from recoiling BHs (Herrmann et al. 2007; Eracleous et al. 2012), tidal disruption events (Gezari 2021), and gas outflows/inflows (Brotherton et al. 1994; Storchi-Bergmann 2010; Rakshit & Woo 2018; Kovačević-Dojčinović et al. 2022). In addition, Barth et al. (2015) found that Hβ velocity centroids can undergo dramatic changes, on timescales of a month, in response to continuum flux variations. The radial velocity shifts in this case are a product of asymmetric reverberation by the BLR, and can appear as false-positive detections in searches for binary black holes.

In this paper, we present observations of an AGN with unusual broad emission-line variability, SDSS J141041.25 +531849.0 (hereafter RM160), found within a broader search for variability in broad emission-line profiles in the recently started Sloan Digital Sky Survey V (SDSS-V, Kollmeier et al. 2017; Almeida et al. 2023). Section 2 describes the sample selection, and our criteria to identify quasars with unusual variability in their broad emission-line shapes and to provide the general characteristics of the object of interest. Section 3 describes the methods we use to quantify the broad emission-line profiles. Section 4 describes the changes in broad emission-line profiles and presents a physical model to explain the observations. Section 5 summarizes our results.

Throughout this work, we assume a ΛCDM cosmology with $\Omega_\Lambda = 0.7$, $\Omega_M = 0.3$, and $H_0 = 70\,{\rm km\,s^{-1}\,Mpc^{-1}}$.

2. Observations and Parent Sample

2.1. Data

The data are from the third (Eisenstein et al. 2011), fourth (Blanton et al. 2017), and ongoing fifth generation (Kollmeier et al. 2017, Almeida et al. 2023) of the Sloan Digital Sky Survey (SDSS, York et al. 2000). The data were obtained using the plate-based, fiber-fed BOSS spectrograph (Smee et al. 2013) mounted on the 2.5 m SDSS telescope (Gunn et al. 2006) at the Apache Point Observatory. The spectrograph has a dual-channel design, a blue channel (3000 Å $< \lambda <$ 6350 Å) and a red channel (5650 Å $< \lambda <$ 10400 Å), both with a spectral resolution of $R \sim 2000$. The SDSS-III and SDSS-IV data (2013–2020) were reduced with the v5_13_0 version of idlspec2d, and the SDSS-V data (2021–present) were reduced with the v6_0_9 version of idlspec2d, the SDSS BOSS spectroscopic reduction pipeline (Bolton et al. 2012).

The spectroscopic monitoring spans a range of nine years (2013–2022) with 127 epochs. An "epoch" generally represents observations taken in a single night, but in some cases epochs will include observations coadded from up to three consecutive nights in order to pass the "epoch completion threshold,"

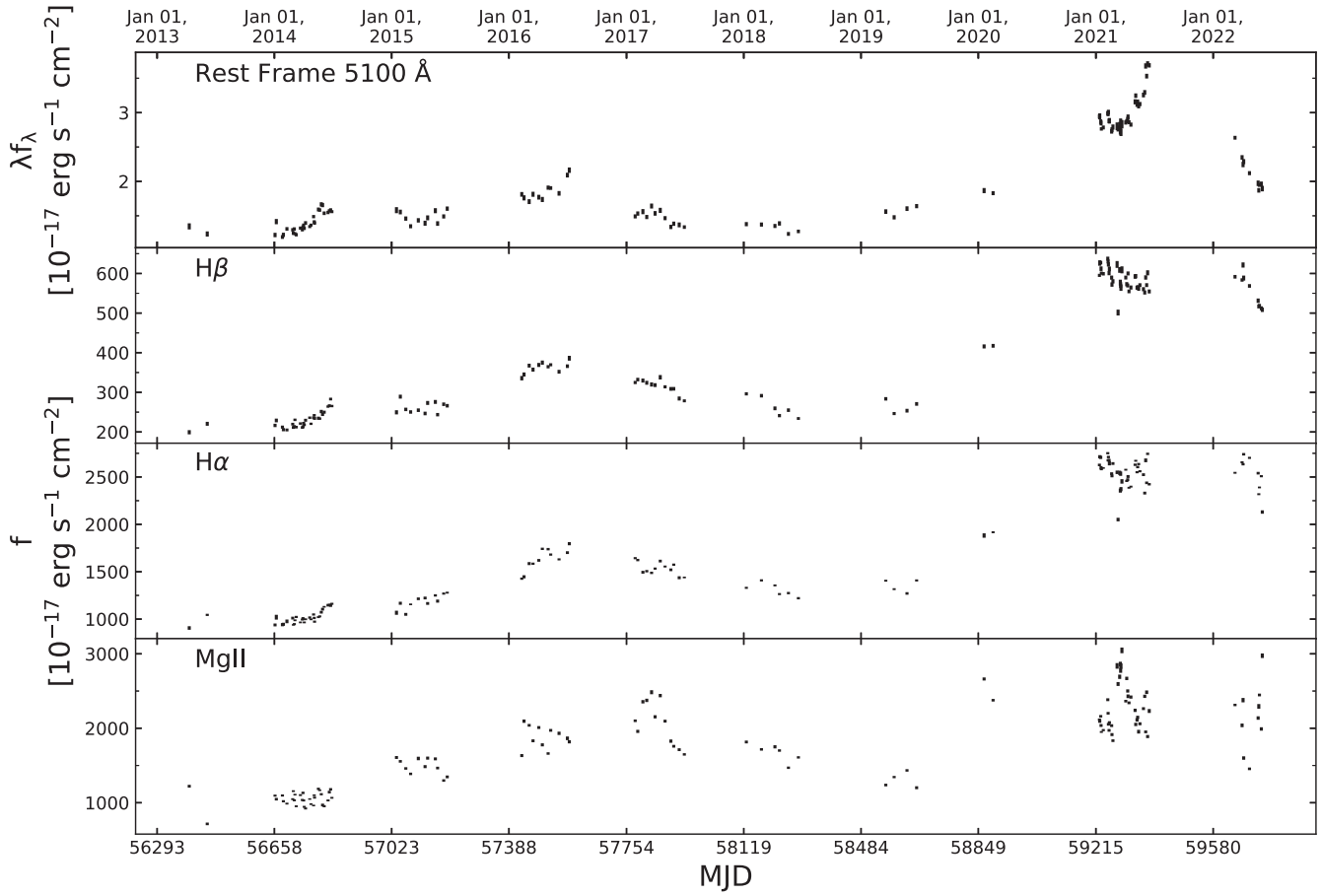

Figure 1. Spectroscopic light curves for the rest-frame 5100 Å continuum and the three emission lines (Hβ, Hα, Mg II). All three of the lines are brightest in the 2021–2022 monitoring period, although Hβ and Hα have more extreme brightening than Mg II. The emission-line variability generally appears to follow the continuum variability with lags consistent with the previously measured $\tau \sim 30$ days for the Balmer lines (Grier et al. 2017b) and $\tau \sim 145$ days for Mg II (Homayouni et al. 2020).

defined as a blue-channel-based signal-to-noise ratio (S/N) threshold of $(S/N)^2(g) > 20$ for a target of fiducial point-spread function (PSF) magnitude $g = 22$. This observing design aims to maintain a constant and useful S/N for all epochs, although some epochs have lower S/N because they could not be completed (i.e., pass the epoch completion threshold) within three nights.

Figure 1 shows the spectroscopic light curves[29] for our quasar of interest, RM160, as a demonstration of the SDSS Reverberation Mapping (SDSS-RM) and SDSS-V Black Hole Mapper Reverberation Mapping (BHM-RM) data sets. The highest density of monitoring from SDSS-III and SDSS-IV occurred in 2014 (30 epochs) and at the start of SDSS-V in 2021 (39 epochs). These light curves include a second-order calibration in flux and wavelength using the [O III] λ5007 narrow emission line (see Section 3.3 for details).

2.2. Parent Sample

The parent sample for our broader unusual variability search consists of all 320 quasars that have been monitored by both the SDSS-V BHM-RM program (for details: see J. R. Trump et al. 2023, in preparation) and SDSS-RM (for details: see Shen et al. 2015, 2019). These targets lie within the SDSS-RM field, which is a 7 deg^2 field that has been observed as a part of SDSS-RM in SDSS-III and SDSS-IV from 2013–2020, and then by BHM-RM in SDSS-V since 2021 (with monitoring scheduled to continue through at least 2026). The parent sample spans a redshift range of $0.1 < z < 4.34$ and is magnitude-limited by $i_{\rm PSF} < 21.7$. The median redshift of the parent sample is $z_{\rm med} = 1.52$ and the median i-band magnitude of the parent sample is $i_{\rm med} = 21.09$.

2.3. Identifying Unusual Changes in Line Profile in SDSS-RM/BHM-RM Quasars

Our object of interest, RM160, was found during a broad search for quasars with variability in their broad emission-line profiles. To measure variability, we quantified changes to the broad emission-line profiles in each epoch using the reduced chi-squared $\chi^2_\nu = \frac{1}{\nu}\sum\frac{(O_i - M_i)^2}{U_i^2}$, with ν the degrees of freedom, O_i the observed flux density, M_i the model flux density (described below), and U_i the observational uncertainty summed across a wavelength range indexed by i.

We use the median spectrum across all 127 epochs as our model flux density in our chi-squared calculation. We seek to identify changes in the line-profile *shape*, rather than the (commonly observed) brightening or dimming of the overall broad line. To accomplish this, we allow the median spectrum in the line-profile region to scale up and down by a multiplicative factor computed from the ratio of the median flux density of the line-profile region at each epoch to the

[29] The observables shown here are explained further in Section 2.4.

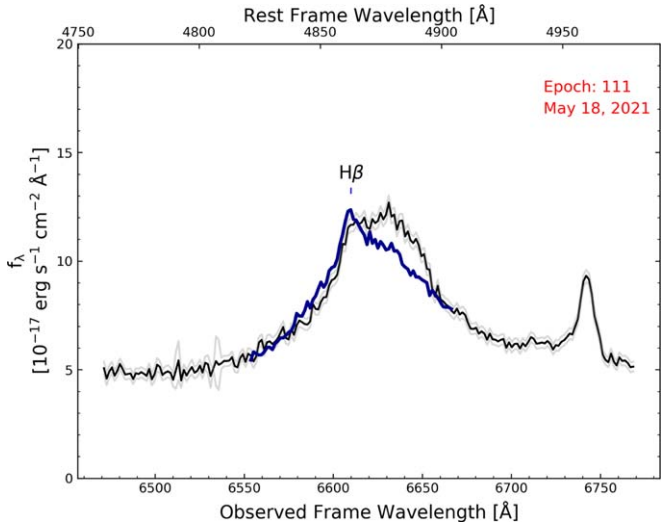

Figure 2. The Hβ spectral region for RM160 in Epoch 111 (2021 May 18, corresponding to MJD 59,352). The dark blue line is the median spectrum computed for the Hβ line centered on the line center and has a total width of 1.5 × FWHM reported by Shen et al. (2019). In this particular epoch the Hβ emission-line profile is redder than the median profile. The online version of this figure is an animation. The animation is 1:00 minutes long and shows the time evolution of RM160 for all 127 epochs of spectra beginning on 2013 April 11 and ending on 2022 June 3.

(An animation of this figure is available.)

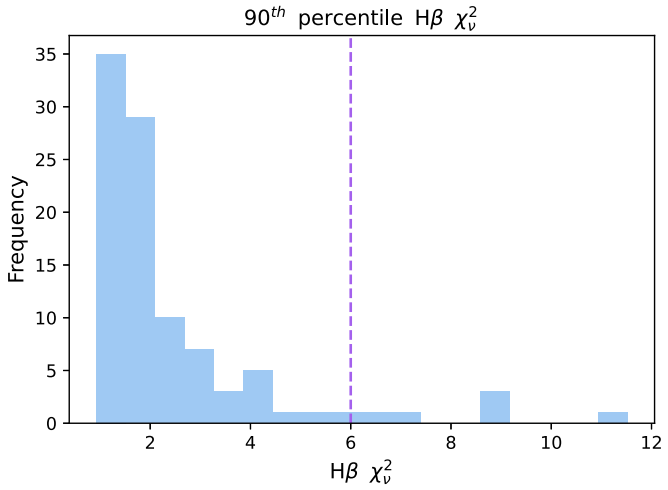

Figure 3. Distribution of $\chi^2_\nu(90\%)$ measured from the multiepoch Hβ region spectra for the 320 objects in our parent SDSS-RM sample. The vertical, dashed purple line indicates our criterion ($\chi^2_\nu(90\%) \geqslant 6$) for identifying unusual line-profile variability. The $\chi^2_\nu(90\%)$ for RM160 is 8.44 and was chosen because it had the highest S/N and the most apparent variability in the broad emission-line profile, while the other ones that satisfied our $\chi^2_\nu(90\%)$ criterion were either noisy and/or had less apparent variability in their broad emission-line profiles.

average flux density of the line-profile region across all epochs. Figure 2 shows an example spectrum for RM160, where the blue line shows the median spectrum centered on the emission-line region and spanning a total width of 1.5 × FWHM reported in Shen et al. (2019), which is the extent to which we measure variability of the broad emission-line profile.

We identified interesting candidates using the 90th percentile of the distribution of the χ^2_ν values from each epoch, choosing $\chi^2_\nu(90\%) > 6$ as a threshold associated with the tail of line-profile variability. Figure 3 shows the distribution of Hβ $\chi^2_\nu(90\%)$ of our sample.

There are 15 objects that fit our $\chi^2_\nu(90\%)$ criterion. We visually inspected the variability of the 15 objects by creating animations of the time-variable spectra for all 127 epochs. Out of those 15 objects, we identified the subject of this study, RM160. The $\chi^2_\nu(90\%)$ for RM160 is 8.44. We noticed from visual inspection that the Hβ, Hα, and Mg II broad emission lines of RM160 all appear to undergo significant velocity shifts over time. The apparent variability of the remaining objects was largely the result of noise.

2.4. The Source of Interest: RM160

The subject of this study is RM160, a luminous quasar ($\lambda L_\lambda(5100\,\text{Å}) = 4.7 \times 10^{44}$ erg s^{-1}) in the SDSS-RM field. It has a redshift of $z = 0.359$ and an i-band magnitude of $i = 19.68$.

There are published Hβ, Hα, and Mg II RM time lags for this object. The Hβ and Hα lags were measured by Grier et al. (2017b) using only the 2014 data. The observed-frame Hβ lag is $\tau_{\text{H}\beta,\text{obs}} = 31.3^{+8.1}_{-4.1}$ days and the observed-frame Hα lag is $\tau_{\text{H}\alpha,\text{obs}} = 27.7^{+5.3}_{-4.7}$ days. The observed-frame Mg II lags were measured in Homayouni et al. (2020) using four years of data (2014–2017). The observed-frame Mg II lag is $\tau_{\text{MgII},\text{obs}} = 144.7^{+24.7}_{-22.6}$ days. We note that the Mg II lag for this object has a false-positive rate of 16%, which is not in the "gold-sample" (false-positive rate of $\leqslant$10%) of Homayouni et al. (2020). As such, the Mg II lag for RM160 may be unreliable. In general, we assume that the Mg II lag is longer than the lags of the Balmer lines (i.e., we assume the BLR is stratified; see Clavel et al. 1991; Reichert et al. 1994). The black hole mass of RM160 was computed in Grier et al. (2017b) to be $(M_{\text{BH}}/10^7 M_\odot) = 7.0^{+1.7}_{-1.3}$.

From Hubble Space Telescope imaging (taken on 2020 September 28), the host-galaxy contribution for RM160 is 14% in F606W (Li et al. 2023). This measurement does not take into account the 2″ SDSS fiber, which would make the host-fraction even smaller, thus we do not account for the marginal host contribution in our analysis and we assume that the spectrum is dominated by the quasar.

Figure 1 shows the continuum and emission-line light curves for RM160. The light-curve behavior appears to be qualitatively consistent with the previously measured lags, with the Balmer-line variability appearing to follow the same pattern as the continuum after a lag of ∼30 days and the Mg II variability following the same pattern after an additional ∼145 days.

3. Quantifying the Emission-line Profiles

3.1. Fitting the Continuum

To isolate and model the broad emission-line regions, we first need to subtract the continuum from the spectra. To subtract the continuum, we fit a first-order polynomial to the spectrum based on the median of the continuum over 50 pixels from the line-free regions blueward and redward of the broad lines (and nearby narrow lines for Hβ and Hα). The continuum fits for the median spectrum are shown in yellow in the top panels in Figure 4. The Appendix presents alternative modeling with `PyQSOFit` (Guo et al. 2018; Shen et al. 2019) that separately fits the continuum and iron pseudo-continuum and finds consistent variability patterns in the fitted line properties.

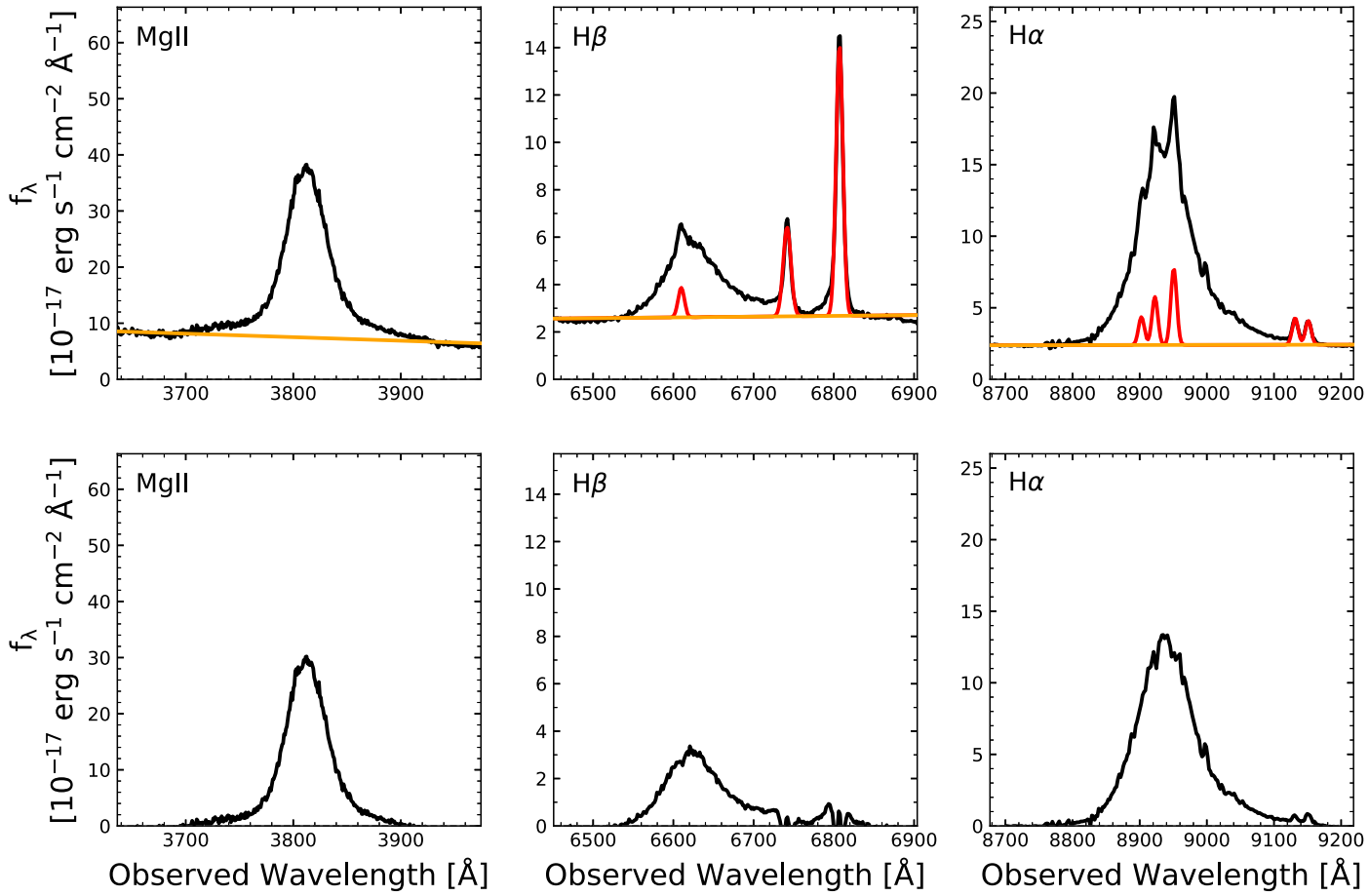

Figure 4. Median spectra for Mg II, Hβ, and Hα of RM160. The top row shows the full spectrum in black along with the narrow emission-line fits in red and the continuum fits in orange. The bottom row shows the continuum- and narrow-line-subtracted median spectra for Mg II, Hβ, and Hα, respectively. Our continuum- and narrow-line-subtracted spectra show clear broad-line profiles (the residuals from non-Gaussian narrow lines do not affect the broad-line measurements).

3.2. Fitting the Narrow Emission Lines

We fit each narrow emission line in the Hα and Hβ regions with a single Gaussian. We assume that the narrow lines are constant over the course of our monitoring period of $\sim$9 yr. In Section 3.3, we confirm this assumption by demonstrating that the [O III] λ5007 narrow-line flux is constant over the monitoring period.

We used the [O III] λ5007 parameters to constrain the other narrow-line fits. Specifically, we tied the line centers of the narrow-line Gaussian fits, for each epoch, to [O III] λ5007 using the narrow-line wavelength centers from Vanden Berk et al. (2001). We also tied the line widths of the narrow-line Gaussian fits, for each epoch, to the line width from the [O III] λ5007 fit. The [O III] λ4959 line flux was also constrained to be 1/3 that of the [O III] λ5007 line flux (Storey & Zeippen 2000).

For each individual fit for the Hα region, we fit the Hα narrow line without constraints on the amplitude and found that this resulted in a clean-looking residual (i.e., a clear broad emission-line profile with the narrow emission lines cleanly subtracted out). However, this unconstrained approach to the narrow Hβ line resulted in poor fits with large apparent residuals. Therefore, we constrained the amplitude of the narrow Hβ line to a value that produced a smooth broad-line residual that lacked a cuspy narrow-line peak in the median spectrum fit. We then applied that narrow Hβ amplitude to the fits for all epochs.

Figure 4 illustrates the process of fitting and subtracting both the continuum and the narrow emission lines. There are limitations to modeling complex spectra with a single Gaussian. For example, the [O III] λ5007 line appears to have a blue wing that cannot be modeled using a single Gaussian and would be better fit with two or more Gaussians. This asymmetric, non-Gaussian profile has been shown to be due to outflowing, ionized gas in the narrow-line region (Rojas et al. 2020; Ayubinia et al. 2022; Molina et al. 2022). However, these small residuals caused by non-Gaussian shapes in the narrow emission lines do not affect the measured broad-line profiles. We visually inspected the fits for each broad emission line in each epoch and confirmed that our method produces clean broad-line profiles that have effective subtractions of the continuum and narrow emission lines.

3.3. Second-order Calibrations Based on Narrow Emission Lines

We investigated the stability of the narrow emission lines to examine and improve the flux and wavelength calibration. The [O III] λ5007 line is observed to be stable over timescales of a few years (Foltz et al. 1981; Peterson et al. 1982) and so it is often used as a flux-calibration standard in AGN spectra. We examine the possibility of applying a spectrophotometric calibration by fitting the [O III] λ5007 line with a single Gaussian in each epoch, which is separate from the aforementioned fitting procedure in Section 3.2. In Figure 5, we show the

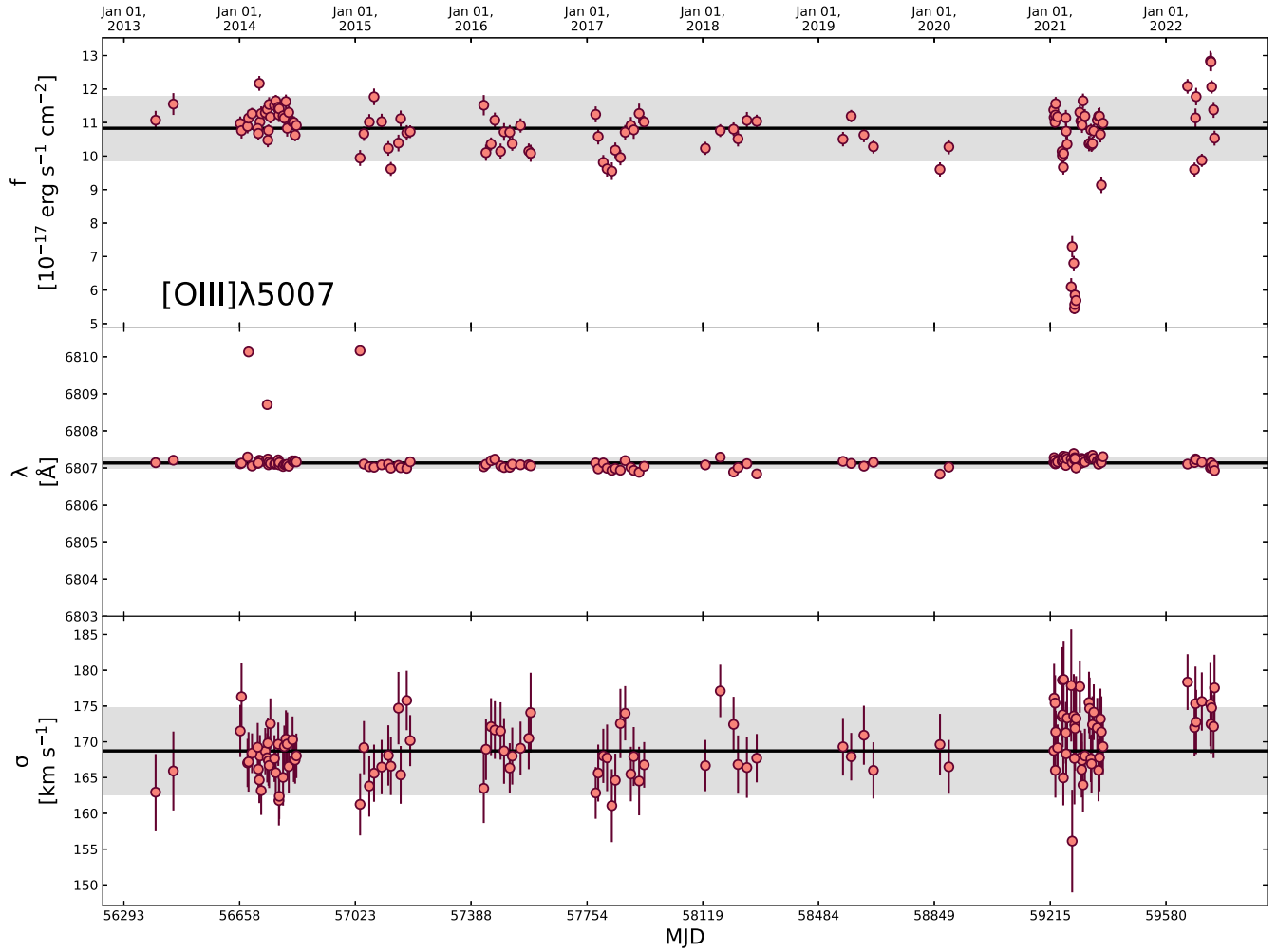

Figure 5. The [O III] λ5007 flux (top), line center (middle), and line width σ (bottom) measured from single-Gaussian fits of the continuum-subtracted spectra at each epoch. In all panels, the black line indicates the median and the gray shading represents the NMAD. We use the apparent changes in [O III] λ5007 flux and line center for a second-order flux and wavelength calibration for the spectra of each epoch.

Gaussian fit parameters for [O III] λ5007 line flux, center, and width, as well as the respective median values (black) and normalized median absolute deviations (NMADs; gray regions). Figure 5 confirms our assumption of a nonvariable [O III] λ5007 line throughout the course of our monitoring period. We note that in the case of NGC 5548, the [O III] λ5007 line has been shown to vary by $\sim$10% over a timescale of $\sim$30 yr (Peterson et al. 2013).

Since the [O III] λ5007 narrow line does not vary over these timescales, the changes in [O III] λ5007 flux represent epoch-dependent changes in the spectrophotometric calibration, with eight epochs in 2021 that fall well below the median. The [O III] λ5007 line center shifts by exactly one or two pixels in three epochs, indicating a shift in the wavelength calibration. The [O III] λ5007 line width is constant within its uncertainties, indicating that the spectral resolution is stable throughout the observations.

We observe similar changes in the fitted line fluxes and centers for the [O II] and [S II] emission lines (with larger uncertainties for these weaker lines). This suggests that the flux and wavelength changes are gray (not wavelength-dependent) and systematic (not intrinsic to RM160). In other words, the flux and wavelength changes observed for [O III] λ5007 represent gray calibration issues for the entire spectrum.

We perform a second-order flux and wavelength calibration that forces the [O III] λ5007 flux and wavelength to be constant across all epochs and apply it to the spectra at each epoch. We scale the spectrum at each epoch by a factor of $\tilde{f}$[O III]$/f$[O III] and we correct the wavelength of each spectrum by a factor of $\tilde{\mu}$[O III]$/\mu$[O III], where $\tilde{f}$[O III] and $\tilde{\mu}$[O III] are the median [O III] λ5007 flux and line center, respectively, across all epochs and f[O III] and μ[O III] are the [O III] λ5007 flux and line center at each epoch.

3.4. Quantifying the Variability in the Broad Emission-line Profile

We measure the broad emission-line properties of the continuum- and narrow-line-subtracted spectra using the moments of a distribution:

1. Line flux: $f = \sum_{\lambda_1}^{\lambda_2} f_\lambda(\lambda)\Delta\lambda$
2. Line center: $\lambda_C = \frac{\sum_{\lambda_1}^{\lambda_2} \lambda f_\lambda(\lambda)\Delta\lambda}{\sum_{\lambda_1}^{\lambda_2} f_\lambda(\lambda)\Delta\lambda}$
3. Line width: $\sigma = \sqrt{\frac{\sum_{\lambda_1}^{\lambda_2}(\lambda_C - \mu)^2 f_\lambda(\lambda)\Delta\lambda}{\sum_{\lambda_1}^{\lambda_2} f_\lambda(\lambda)\Delta\lambda}}$
4. FWHM: we measured FWHM by first applying a median boxcar smoothing of 5 pixels to our spectra at each

epoch. We then used the FWHM routine from the `specutils` package (Earl et al. 2022) to compute the FWHM.

Here f_λ is the flux density, λ is the wavelength, $\Delta\lambda$ is the wavelength per pixel, and λ_1 and λ_2 for each line are from Vanden Berk et al. (2001). These nonparametric measurements were chosen because they make no assumptions about the underlying shape of the broad-line profiles. We used the nonparametric model on the continuum- and narrow-line-subtracted spectra (bottom panels in Figure 4).

We employ a Monte Carlo resampling approach to estimate the uncertainties in line flux, line center, and line width (both σ and FWHM). For each epoch, we measured these quantities for 200 resampled spectra using the corresponding error spectrum. We adopted the standard deviations in the measured parameters from the 200 resampled spectra as our uncertainties for each epoch.

To test the robustness of our nonparametric measurements, we employed two alternative parametric fitting procedures: (1) using single Gaussians to model the broad emission lines and (2) using `PyQSOFit`, which models the Fe II psuedo-continuum and fits multiple Gaussians to the broad and narrow emission lines. The different methods all show the same relative variability of the broad-line profiles, with the exception of the σ measurements from `PyQSOFit` (for details, see the Appendix). For clarity, we use the nonparametric measurements for our analysis throughout the text.

4. Results and Discussion

4.1. Variability in the Broad Emission-line Profile

Figures 6, 7, and 8 show the variability of the Mg II, Hβ, and Hα broad emission-line profiles as quantified by our nonparametric measures of line flux, line width (FWHM and σ), and line center. In general, in each of the figures, the broad emission lines get brighter and narrower, then fainter and broader, and then brighter and narrower again, with an anticorrelation between the line flux and line width. This phenomenon is known as "line breathing" and we discuss it in more detail in Section 4.2. We note that the line flux and line width (FWHM and σ) of Mg II appear to vary as a lagged version of the Balmer lines, consistent with the observed lags in each emission line of this quasar presented in Grier et al. (2017b) and Homayouni et al. (2020). This suggests that the Mg II-emitting region is further away from the central engine than the Balmer-emitting regions.

All three broad emission lines have line centers that are much redder than the systemic redshift, as determined from the narrow emission lines. The broad-line centers all have a similar general variability pattern of starting red, shifting bluer over a few years, and then getting redder near the end of our monitoring period. The broad Hβ line is redder than the other broad lines and has the largest radial velocity shifts (maximum change in Δv of $\sim$800 km s^{-1}, compared to $\sim$400 km s^{-1} for Hα and Mg II). All three lines become bluest (but still redder than the systemic narrow-line redshift) in about 2017 and become red again by about 2020, with Mg II returning to its initial red center while Hα and Hβ do not become as red as when they started.

Unlike the light curves of the emission-line flux, the comparison between the radial velocity shifts in the Balmer lines (Hβ and Hα) and Mg II is inconsistent with the measured lags reported by Grier et al. (2017b) and Homayouni et al. (2020). Specifically, the Mg II radial velocity shifts do not appear to mirror the Balmer-line shifts after a lag of $\sim$100 days. Instead, the Mg II radial velocity shifts appear to be a smoother version of the Balmer-line shifts with no apparent lag between them.

The radial velocity shifts of RM160 are qualitatively similar to, but more extreme than, what is observed for the lower-luminosity Seyfert 1 AGN discussed by Barth et al. (2015). For example, the largest shifts reported by Barth et al. (2015) are for NGC 4593, with radial velocity shifts of 266 ± 11 km s^{-1} for the broad Hβ emission line. RM160 has a much more dramatic Hβ velocity shift of $\sim$800 km s^{-1}, which occurs over $\sim$4 years. Sergeev et al. (2007) studied NGC 5548 and found radial velocity shifts of $\sim$1000 km s^{-1} over a 30 yr period.

4.2. Line Breathing

Line breathing is an anticorrelation between the flux and the width of a broad emission line over time that has long been predicted by photoionization modeling (Korista & Goad 2004). Gas in a Keplerian orbit, as is the likely case for the BLR, has higher velocity at small radii and lower velocity at large radii. For BLR gas ionized by a central continuum, an increase in the continuum flux will overionize the gas nearest to the black hole and will thus increase the emissivity-weighted BLR radius. The increase in the optimal emitting radius will result in a decrease in the line width, since gas orbiting at a larger radius has a lower orbital velocity. Observations have shown that BLR line breathing can occur on timescales of days to weeks (Barth et al. 2015). Line breathing is described by the following relation:

$$\Delta \log W = \beta\, \Delta \log L \tag{2}$$

where W is the line width, L is the broad emission-line luminosity, and β is some constant of proportionality. The broad-line luminosity is generally used for L in Equation (2) as a (lagged) representation of the continuum luminosity that is responsible for driving the change in optimal emitting radius. Assuming a typical radius–luminosity relationship of $R_{\rm BLR} \propto L^{0.5}$ (Bentz et al. 2013) and virial orbits ($v \propto R_{\rm BLR}^{-0.5}$), the expected relation between the changes in line width and broad emission-line luminosity is $\Delta \log W = -0.25\, \Delta \log L$.

Reverberation mapping studies over time have shown that line breathing is observed for Hβ (Cackett & Horne 2006; Park et al. 2012; Barth et al. 2015; Wang et al. 2020), typically consistent with the expected constant of proportionality of $\beta = -0.25$. On the other hand, observations of Mg II have found weak or no anticorrelations between line width and flux (Dexter et al. 2019; Homan et al. 2020; Yang et al. 2020; Wang et al. 2020). In C IV, some observations have found a "reverse breathing" effect whereby the line width of C IV increases with increasing flux (Wilhite et al. 2006; Wang et al. 2020). Furthermore, Wang et al. (2020) found that Hα shows much less breathing than Hβ on average. The differences in line breathing patterns between broad emission lines indicate that there could be a difference in the distribution of the gas around a particular "optimal emitting region" and can also indicate that the structure of the BLR is not uniform at all radii. Studying line breathing behavior for different emission lines can give clues about the multiscale structure of the BLR.

We analyze line breathing for the three major broad lines accessible in RM160 (Mg II, Hβ, and Hα) over the entire 9 yr

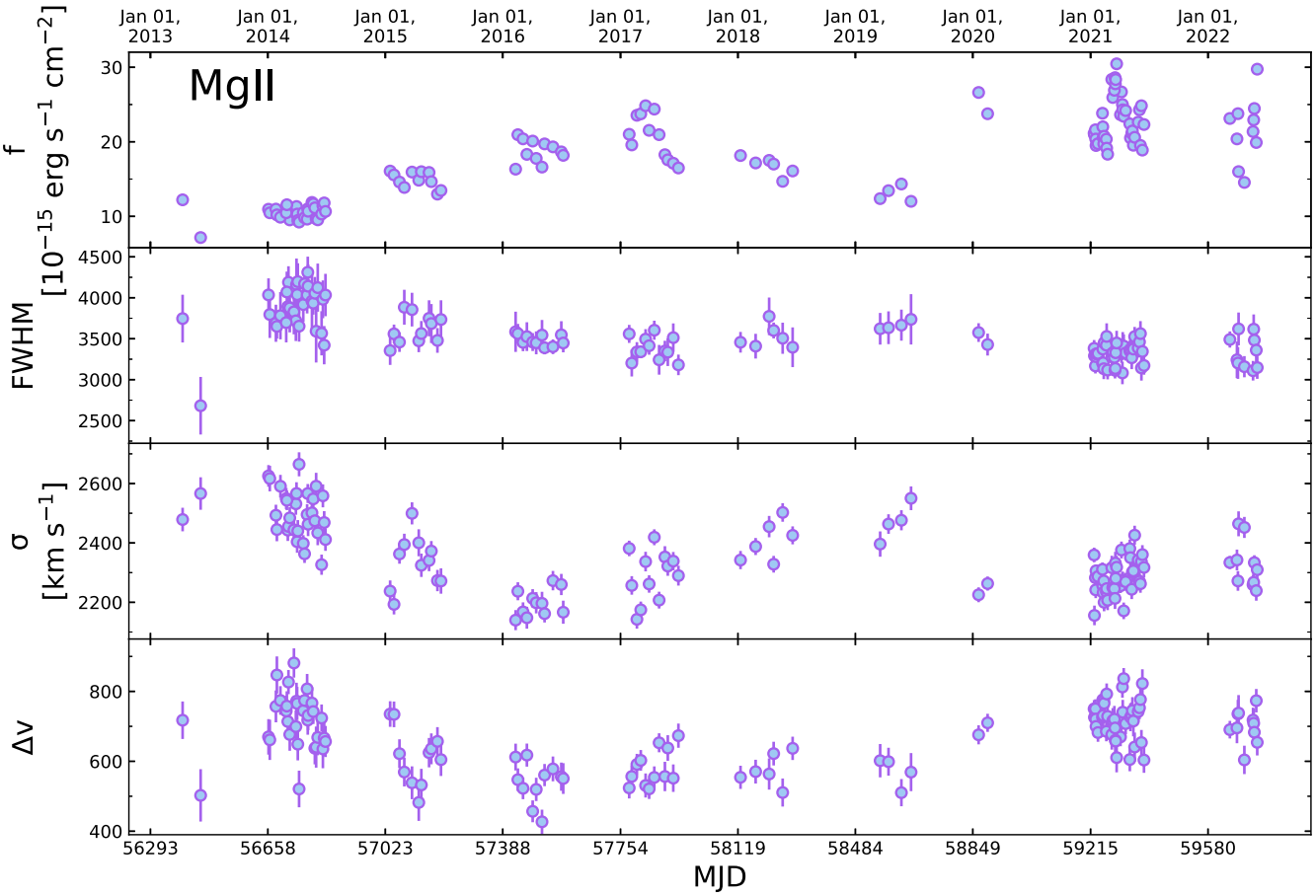

Figure 6. Variability of the Mg II broad emission-line profile, as quantified by our nonparametric measurements of the line flux (top row), FWHM (second row), line width σ (third row), and the line-center velocity shift Δv (bottom row). The FWHM, line width σ, and line-center velocity shift Δv are all in units of km s^{-1}. The Mg II line gets brighter and narrower, then fainter and broader, and then brighter and narrower again. Meanwhile, the line center starts very red (compared to the systemic redshift from the narrow emission lines), gets bluer, and then gets as red as it was at the beginning. The velocity shifts in the line center do not appear to be simultaneously correlated with the changes in line flux and line width.

monitoring period studied here (2013–2022). Figure 9 shows the relationship between broad-line width (FWHM and σ) and broad-line flux for Mg II, Hβ, and Hα. We fit the lines with linear models, motivated by Equation (2), using the Bayesian linear regression package `linmix` (Kelly 2007). The slopes (β) determined from `linmix` are shown in Figure 9 at the bottom left. All three emission lines exhibit an anticorrelation between broad-line width and broad-line flux, with a slope that is steeper for FWHM and shallower for σ. The Hβ line has the steepest anticorrelation and Mg II has the shallowest anticorrelation, in general agreement with previous work (Wang et al. 2020).

The line breathing properties of RM160 were previously measured by Wang et al. (2020) using the continuum flux and broad-line widths from 29 epochs of spectra observed over 2014–2017 (choosing only epochs that are 2σ above the mean S/N of each season from the 64 total epochs in 2014–2017). Our study measures the line breathing properties over a longer period with 127 epochs of spectra over 2013–2022 using the respective broad-line flux, which is a lagged representation of the continuum flux, and broad-line widths. Table 1 compares the line breathing relationship, characterized by the slopes between the widths and fluxes, from the present study (using broad emission-line width and broad emission-line flux) to Wang et al. (2020) (using broad emission-line widths and continuum flux).

We find almost identical results for β_σ (slope for σ line width) for Mg II and Hα, and β_σ is fairly close for Hβ. However, we see large disparities in $\beta_{\rm FWHM}$ for all three broad emission lines, likely due to the differences in flux (continuum versus broad-line) used in the analyses.

In Figure 9, there are distinct differences in the line breathing slopes measured from line width σ and FWHM. We investigate the differences in FWHM and σ further in Figure 10, which shows the ratio of FWHM to σ as a function of time with a color bar indicating the relative broad emission-line flux at each epoch. The FWHM/σ ratio measures the boxiness/peakiness of an emission line, with FWHM/$\sigma = 2.355$ for a Gaussian, a higher ratio (FWHM/$\sigma > 2.355$) for a boxy line (i.e., low kurtosis), and a lower ratio (FWHM/$\sigma < 2.355$) for a peaky line (i.e., high kurtosis). The Mg II line in RM160 becomes slightly peakier with time (and with increasing flux). The Balmer lines change much more dramatically, going from Gaussian or boxy profiles at a low flux at the beginning of the monitoring to much peakier profiles at late times and high fluxes.

The change from boxier to peakier broad-line profiles explains the difference in line breathing slopes measured for FWHM and σ. The changes in received continuum (as measured in the varying emission-line flux) do not drive monolithic changes in the observed BLR orbits of RM160, and instead result in changes to the shape of the velocity

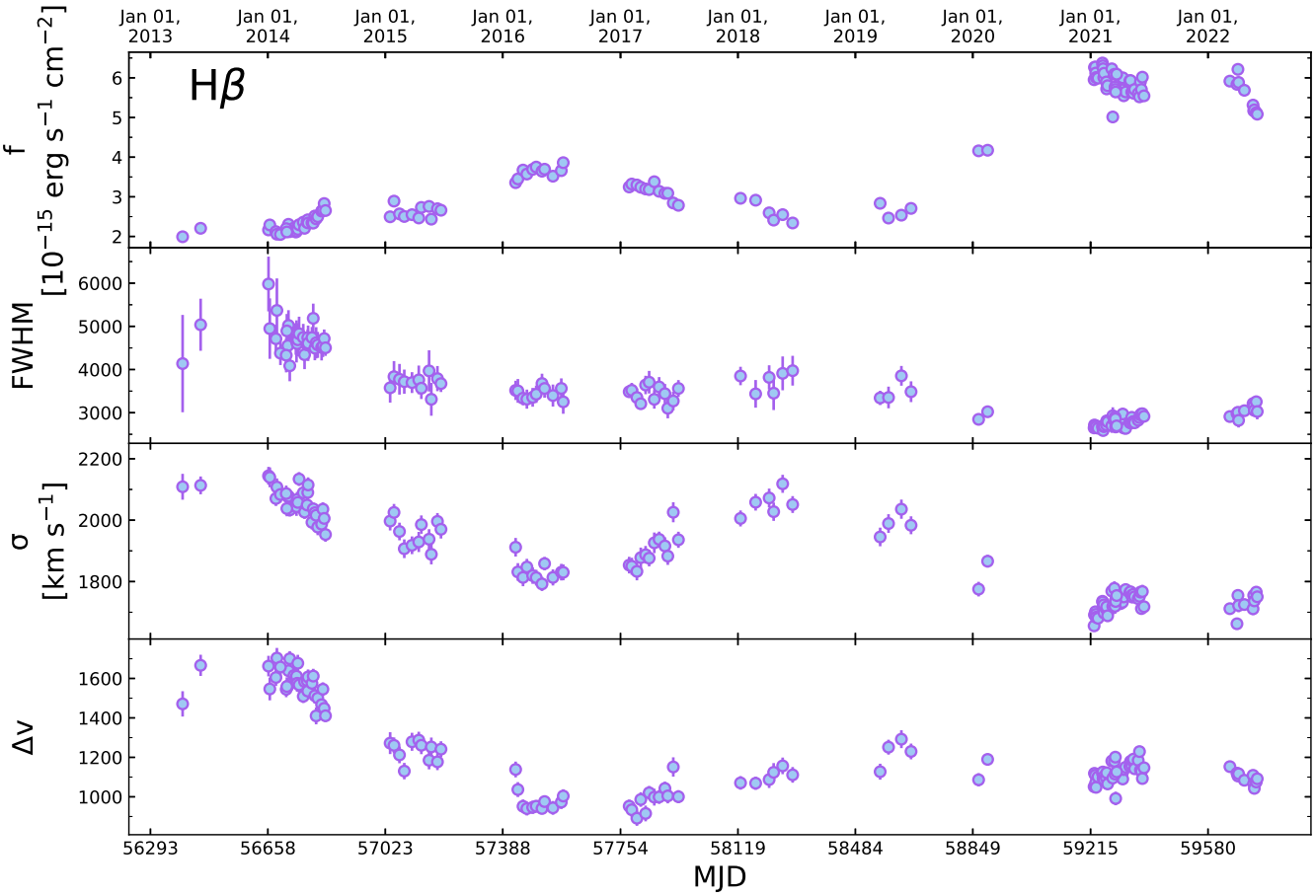

Figure 7. Variability of the Hβ broad emission-line profile, as quantified by our nonparametric measurements of the line flux (top row), FWHM (second row), line width σ (third row), and the line-center velocity shifts Δv (bottom row). The FWHM, line width σ, and line-center velocity shift Δv are all in units of km s^{-1}. The Hβ line gets brighter and narrower, then fainter and broader, and then brighter and narrower again. Meanwhile, the line center starts very red (compared to the systemic redshift from the narrow emission lines), gets bluer, and then gets more redder and seems to plateau after the 2019 monitoring period. The velocity shifts in line center do not appear to be simultaneously correlated with the changes in line flux and line width.

distribution. This likely indicates asymmetry in the radial distribution of the broad-line gas where a greater contribution from distant, low-velocity gas increases the line core and makes it appear peakier in the luminous phase. We return to a discussion of the complex kinematics of the BLR of RM160 in Section 4.4.

4.3. The Binary Supermassive Black Hole Hypothesis

A periodic Doppler shift of the broad emission lines could be indicative of an SMBH binary (Eracleous et al. 2012). However, in the binary scenario, Δv should be consistent through the different broad emission lines as the systemic velocities should all trace the center of gravity of the active SMBH. This contradicts the observations of RM160 (see Figure 11), where Δv is different for the different broad lines. The differences in Δv for different lines provide evidence to disfavor an SMBH binary as the cause of the radial velocity variations of RM160. The simplest binary scenario (i.e., a scenario in which only one SMBH is active), should also have only bulk radial velocity shifts of the broad emission lines with no variability in their shapes (Figure 1 in Guo et al. 2019), contradicting the FWHM/σ variations observed in our observations (Figure 10). A binary scenario with velocity shifts driven entirely by periodic Doppler motion would also have a Δv curve that is symmetric about zero, opposite in shape (concave down) to our observed (concave up) Δv curves.

We provide further evidence against the binary hypothesis by considering the relationship between binary separation and orbital period (Kepler's third law):

$$a^3 = \frac{GM}{4\pi^2}P^2 \tag{3}$$

where a is the binary separation, G is the gravitational constant, M is the total binary mass, and P is the period of the binary.

There are two possibilities for a binary SMBH system that has a BLR undergoing radial velocity shifts: a close-pair binary with a circumbinary BLR ($a \ll R_{\rm BLR}$ and $P \ll P_{\rm BLR}$) or a wide-separation binary in which each SMBH has its own BLR ($a \gg R_{\rm BLR}$ and $P \gg P_{\rm BLR}$). A binary SMBH with a separation similar to the BLR ($a \approx R_{\rm BLR}$) would disrupt the orbiting gas, and such a system would not have observable broad emission lines (unlike RM160).

In Figure 11, we fit the radial velocity shifts of all three broad emission lines using a sine function with the `LMFIT` package (Newville et al. 2014). The best-fit sine functions have characteristic periods of P(Mg II) $= 16.5 \pm 7.1$ yr, P(Hβ) $= 5.8 \pm 4.2$ yr (or P(Hβ) $= 14.4 \pm 3.4$ yr if fit to only the 2014–2020 data), and P(Hα) $= 22.1 \pm 1.0$ yr.

Using Equation (3) and assuming that the RM mass ($\log(M_{\rm BH}/M_\odot) = 7.8$) for RM160 is the total binary mass

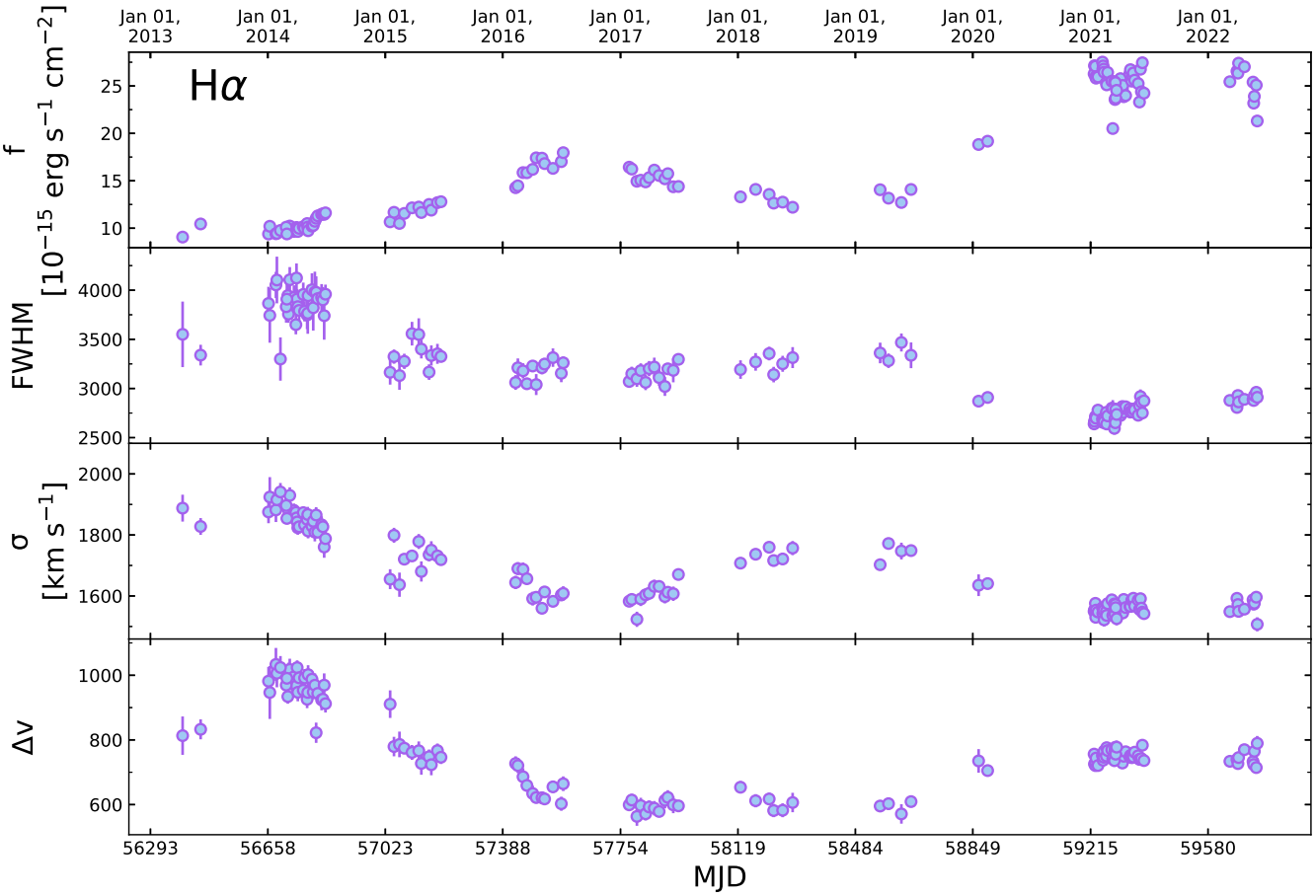

Figure 8. Variability of the Hα broad emission-line profile, as quantified by our nonparametric measurements of the line flux (top row), FWHM (second row), line width σ (third row), and the line-center velocity shifts Δv (bottom row). The FWHM, line width σ, and line-center velocity shift Δv are all in units of km s^{-1}. The Hα line gets brighter and narrower, then fainter and broader, and then brighter and narrower again. Meanwhile, the line center starts very red (compared to the systemic redshift from the narrow emission lines), gets bluer, and then gets more redder, but not as red as it was in the 2014 monitoring period. The velocity shifts in line center do not appear to be simultaneously correlated with the changes in line flux and line width.

(which is the case for the binary scenario with a circumbinary BLR) and that the radial velocity shifts correspond to the period of the binary, the best-fit periods imply binary separations of a(Mg II) $= 14.9 \pm 8.5$ lt-day, $a(\mathrm{H}\beta) = 7.4 \pm 6.0$ lt-day (or a(Hβ) $= 13.6 \pm 5.2$ lt-day if fit to only the 2014–2020 data), and $a(\mathrm{H}\alpha) = 18.1 \pm 2.3$ lt-day. We also use Equation (3) to calculate BLR periods using BLR radii equal to the measured reverberation lags from Grier et al. (2017b) for the Balmer lines and from Homayouni et al. (2020) for the Mg II line. These periods are shown on the top right of each panel in Figure 11.

The best-fit sine periods range from 6 to 22 yr, with semimajor axes of 7 to 18 lt-day for the implied binary orbit. Comparing these values to the observed lags from Grier et al. (2017b) and Homayouni et al. (2020), we find that the range of binary semimajor axis is similar to the observed lag for Hα (i.e., $a_{\mathrm{BLR,H}\alpha} = 27.7^{+5.3}_{-4.7}$ lt-day). In the binary scenario this would place the black hole orbit within the BLR, which would cause the BLR to become unstable due to the gravitational interactions with the orbiting black hole. We therefore disfavor a binary explanation for the radial velocity shifts in RM160.

If we instead consider the possibility of a wide-separation binary system with a BLR around one (active) black hole, then the RM mass represents a minimum for the total binary mass and the semimajor axes from Equation (3) are also minimum values. Even for a maximum total binary mass of 5×10^{10} $M_\odot$ (the upper limit for an AGN, e.g., King 2016) and an extreme binary mass ratio of ∼1000:1, the binary separation would be a(Mg II) $= 166.8 \pm 5.1$ lt-day, again overlapping with the observed BLR size of $a_{\mathrm{MgII}} = 106$ lt-day (Homayouni et al. 2020). In other words, the binary hypothesis is ruled out for both a circumbinary BLR and a single-AGN BLR due to overlap between the putative binary orbit and the observed BLR size.

4.4. BLR Kinematics and Geometry

We begin by calculating the dynamical timescale for the BLR, $\tau_{\mathrm{dyn}} \simeq (R^3_{\mathrm{BLR}}/GM_{\mathrm{BH}})^{1/2} = 7.7$ yr, using the Hβ-based parameters for R_{BLR} and M_{BH}. The best-fit variability periods in Figure 11 are longer than this dynamical timescale, indicating that the observed variability is consistent with dynamical changes in the BLR. We present an example of a phenomenological model for these dynamical changes below.

RM160 has large (∼400–800 km s^{-1}) radial velocity shifts in its broad emission lines. Although the source exhibits line breathing in a fashion that is similar to other quasars, its line shifts do not follow the same pattern as the changes in line brightness and width. One plausible explanation of the radial velocity shifts is a BLR with azimuthal asymmetry and a gradient of inflow velocity in the radial direction. An inflow model is motivated by previous velocity-resolved reverberation mapping observations (e.g., Bentz et al. 2010a, 2021;

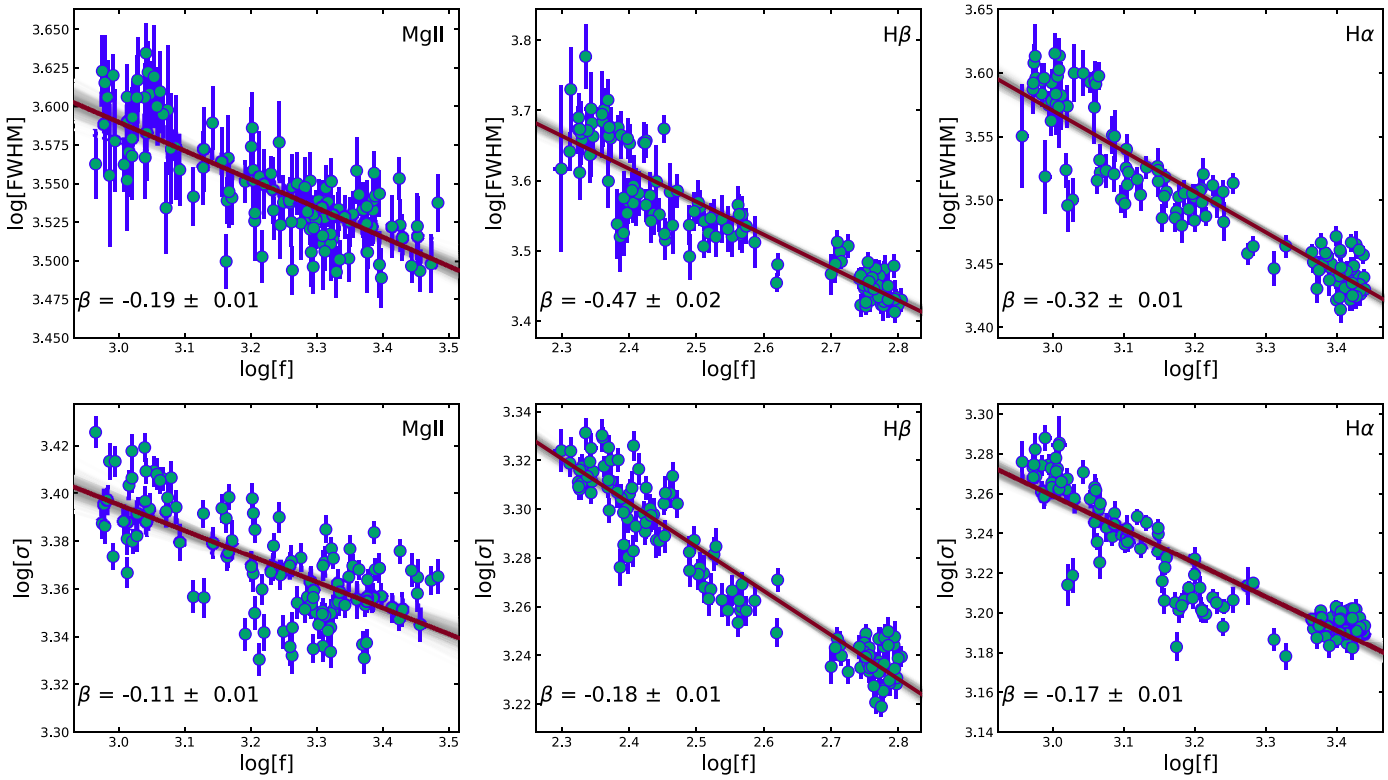

Figure 9. Relationships between line width and line flux for RM160. The green points are the data over our 9 yr monitoring period. The maroon line is the best-fit linear relation and the gray shading indicates the distribution of best-fit lines from the Markov Chains used for the fitting. The top panels show the line FWHM vs. line flux for Mg II, Hβ, and Hα (left to right). The bottom panels show the line width computed from the second moment vs. line flux for Mg II, Hβ, and Hα (left to right). Line widths (FWHM and σ) are in units of km s^{-1} and line fluxes are in units of 10^{-17} erg s^{-1} cm^{-2}.

Table 1
Comparison of the Best-fit Slopes of the Relationship between Broad-line Width (both FWHM and σ) and Flux (Broad-line Flux for our Study and Continuum Flux for Wang et al. 2020)

	Mg II		Hβ		Hα	
Study	$\beta_{\rm FWHM}$	β_σ	$\beta_{\rm FWHM}$	β_σ	$\beta_{\rm FWHM}$	β_σ
Wang et al. (2020)	-0.06 ± 0.01	-0.08 ± 0.01	-0.08 ± 0.01	-0.08 ± 0.01	-0.09 ± 0.01	-0.16 ± 0.01
This work	-0.19 ± 0.01	-0.11 ± 0.01	-0.47 ± 0.02	-0.18 ± 0.01	-0.32 ± 0.01	-0.17 ± 0.01

Note. We note that the results match very well for the Mg II and Hα σ slopes, but the FWHM slopes for Mg II, Hβ, and Hα have large disparities. The differences between slopes measured by Wang et al. (2020) and this study are likely due to changes in line profile between 2014–2017 and 2018–2022, differences in fitting methods, and the difference in flux (broad-line versus continuum) used.

Grier et al. 2017a; U et al. 2022; Villafaña et al. 2022) that frequently find evidence for inflowing BLRs in nearby Seyfert AGNs. Alternatively, we could be seeing an outflow due to BLR emission being preferentially emitted back toward the ionizing source (Ferland et al. 1992), with a gradient of outflow velocity decreasing with radial distance from the quasar. We refer to an inflow hereafter, but acknowledge that a decelerating outflow with the right azimuthal asymmetry might also explain the observations.

Our model is illustrated by Figure 12, which includes an animation of the BLR and its kinematics connected to the observed broad-line light curves and widths.

We begin by noting that all three emission lines have large redshifts ($\sim$500–1600 km s^{-1}) with respect to the narrow lines (i.e., the systemic redshift) at all epochs. This likely indicates bulk *inflow* of the BLR gas in the line of sight. At all epochs the Hβ line is most redshifted ($\sim$900–1600 km s^{-1}) and the Mg II line is the least redshifted ($\sim$500–800 km s^{-1}). The reverberation lags indicate that the Mg II-emitting gas (rest-frame $R_{\rm BLR} = 106$ lt-day; Homayouni et al. 2020) is much further from the continuum emission than the Hβ-emitting gas (rest-frame $R_{\rm BLR} = 23$ lt-day; Grier et al. 2017b). This further implies that the inflow of the BLR gas has a radial gradient, with higher inflow velocity for gas closer to the SMBH (like the Hβ emission region) and lower inflow for more distant gas (like the Mg II emission region). The Hα line is a bit puzzling in this picture because it has a similar reverberation lag (rest-frame $R_{\rm BLR} = 20$ lt-day; Grier et al. 2017b) to Hβ but has a smaller inflow velocity. In general the Hα line is expected to be emitted from slightly larger radii than Hβ due to radial stratification and optical depth effects (Netzer 1975; Rees et al. 1989; Korista & Goad 2004; Bentz et al. 2010b) and we assume that this is also the case here, despite the similarity in measured reverberation lags for the two lines.

Alternatively, the redshifted broad emission lines might be explained by gravitational redshift (Tremaine et al. 2014). This scenario similarly predicts that the Hβ line would be more redshifted than the Hα and Mg II lines, due to Hβ being emitted

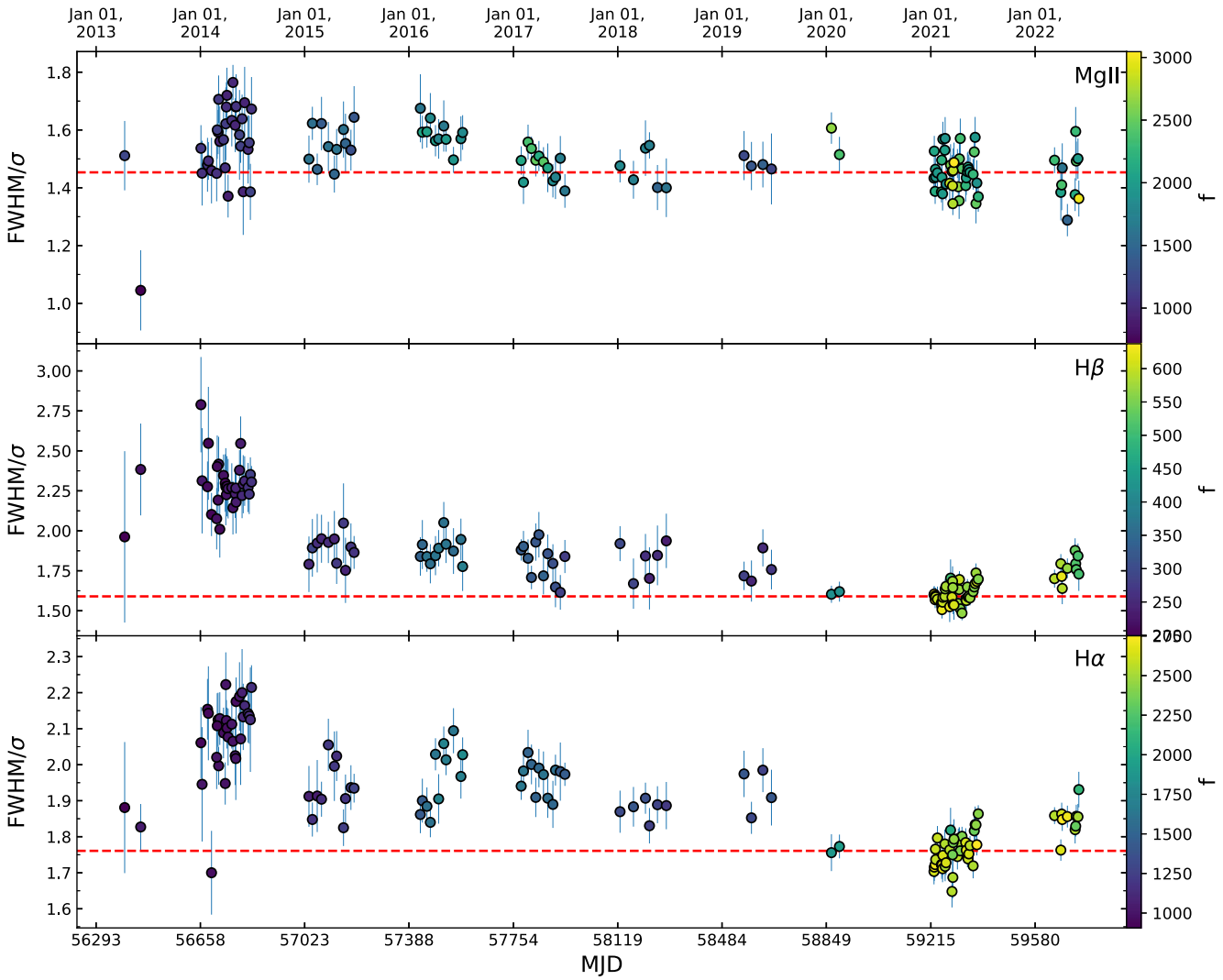

Figure 10. Ratio of FWHM and σ vs. MJD as quantified by our nonparametric measurements of FWHM and σ for Mg II (top row), Hβ (middle row), and Hα (bottom row). The dashed red line indicates the median FWHM/σ value for the 2021 monitoring period and the color bar represents the integrated flux for each emission line in units of 10^{-17} erg s^{-1} cm^{-2}. The ratio of FWHM and σ indicates the peakiness of the distribution. FWHM/$\sigma = 2.355$ would indicate a Gaussian distribution, while a value higher than 2.355 would indicate a boxier line and a value lower than 2.355 would indicate a cuspier line. We see that the peakiness of Mg II is relatively stable over our 9 yr monitoring period, while Hβ and Hα become peakier with time and as they get brighter.

from gas closer to the black hole that has larger orbital velocities. However the broad emission line widths ($\sigma < 3000$ km s^{-1} for all three lines) do not imply relativistic orbits unless the BLR is observed at a nearly face-on inclination. We thus prefer an inflow as the explanation for the redshifted broad emission lines rather than gravitational redshift.

An inflowing BLR explains the redshifted lines, and a radial gradient inflow explains the difference in redshift from Hβ to Hα to Mg II. But it does not explain the *variability* of the broad-line centers. Figure 11 shows that the observed line-center variations, especially for Hα and Mg II, are best fit by a sine function with a period that is similar to the BLR orbital period implied from the Hβ lag (i.e., 22.1 yr for Hα and 16.5 yr for Mg II). This suggests that the line-center shifts might be related to an azimuthal asymmetry in the broad-line emission that orbits the central SMBH. The asymmetric BLR emission might be associated with a higher density in the gas, a hot spot (or hot "wedge" or spiral arm), higher responsivity of the gas on one side or with asymmetric illumination from the accretion disk.

The detailed radial velocity shifts can be explained by a combination of inflowing gas onto the BLR with a radial gradient, orbiting asymmetric gas emission, and flux-driven changes to the optimal emission region (line breathing). At the start of our monitoring in about 2014, the BLR receives low continuum flux and the emission region is close to the SMBH, with high bulk inflow velocity and an asymmetric gas region that is additionally on the receding (redshifted) side of its orbit. The asymmetric gas region reaches the approaching part of the orbit in about 2017, although the line is still redshifted due to the bulk inflow. The modest ($\sim$2$\times$) brightening of the line emission and coordinated decrease in line width over 2014–2017 cause the line emission region to move slightly outward, also resulting in slightly lower redshift of the line. After 2017 the asymmetric region of the BLR begins receding again, and together with the decrease in line flux (and increase in line width, and decrease in emission radius) the line once again becomes redder. We hypothesize that, in about 2020, the orbit of the asymmetric region would have caused the lines to reach the high redshifts they began with in 2014, if not for the

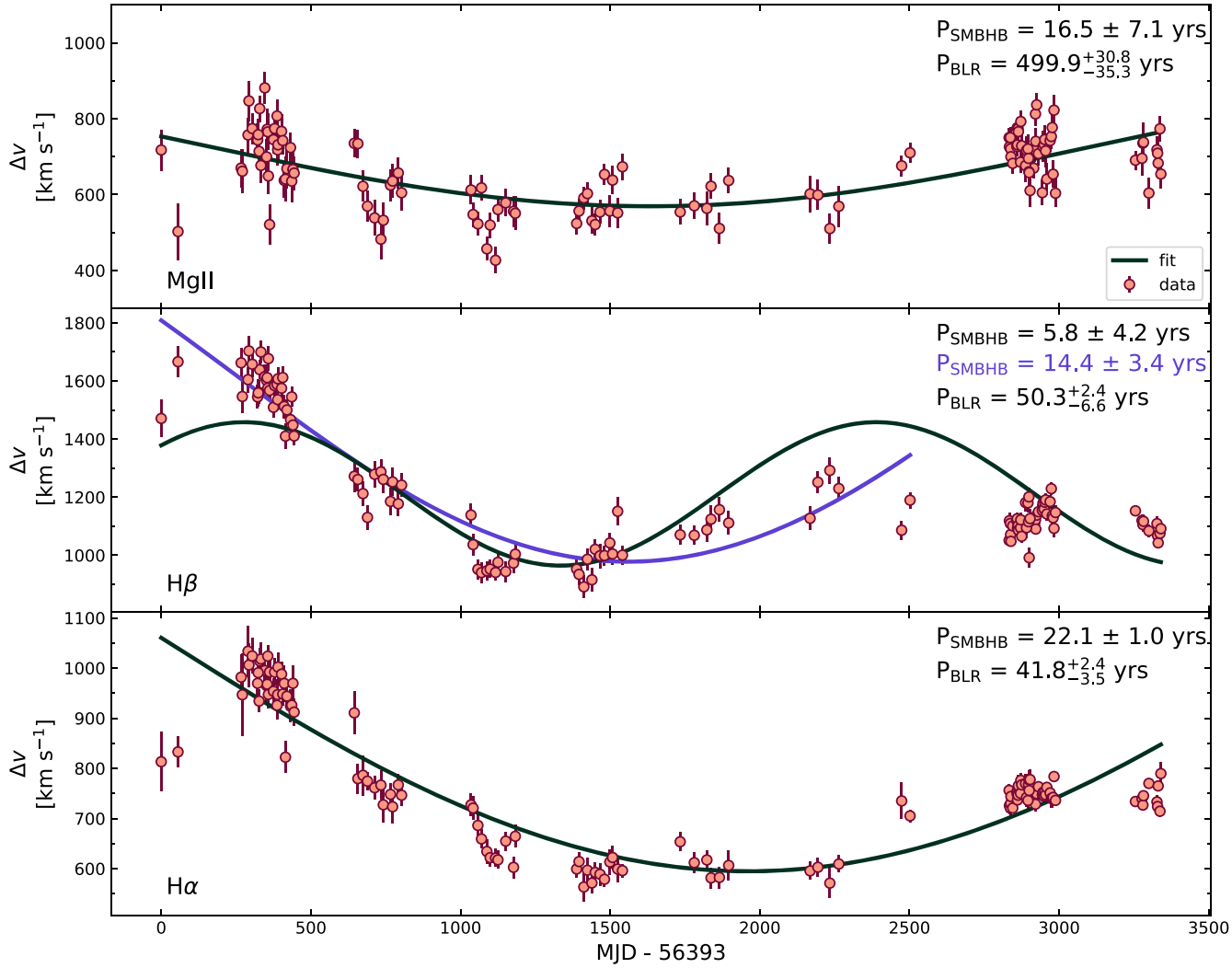

Figure 11. Sine fits to the radial velocity shifts of Mg II (top panel), Hβ (middle panel), and Hα (bottom panel). The tangerine points represent the observations and the black line is the best-fit sine function using the fitting routine `LMFIT` (Newville et al. 2014). The purple line in the middle panel is the best-fit sine function for the Hβ radial velocity shifts excluding the 2021 and 2022 data (MJD – 56393 $<$ 2555). For each emission line, we present the period of the best-fit sine function and the period of the BLR at the top right of each panel. We disfavor a binary explanation for the radial velocity variations because the binary period is similar to the broad-line orbital period, and because the three lines have best-fit sine functions with different periods.

dramatic brightening of the Balmer lines observed in 2020. The significant increase in flux results in the line emission region becoming larger (with observed lower line widths), corresponding to lower bulk inflow velocities. Combined with the redder emission from the orbiting azimuthal asymmetry, the decreased bulk inflow velocity results in a lower integrated redshift velocity for the line in 2020 as compared to 2014.

The combined effects of bulk inflow, azimuthal asymmetry, and line breathing are strongest for Hβ, as the line is at a smaller $R_{\rm BLR}$, and weakest for Mg II, as the line is at a much larger $R_{\rm BLR}$. Over 2014–2020 the Mg II line-center shifts are much more symmetric than the Hβ line-center shifts. The Hβ line also has much larger redshift velocities than the other lines due to its emission region occupying smaller BLR radii.

Velocity-resolved reverberation mapping would provide a test of our geometric and kinematic model for the BLR in RM160 shown in Figure 12. Velocity-resolved RM involves measuring how different segments of an emission line reverberate in response to continuum variations (Denney et al. 2009; Bentz et al. 2009, 2010b; Li et al. 2022; Villafaña et al. 2022; U et al. 2022). If the BLR is virialized, the lags at the center of the emission line are the longest since they preferentially correspond to gas further from the black hole, with shorter lags measured for the line wings. For an inflowing BLR (like our phenomenological model), the lags of the blue wing would be longest and the lags of the red wing would be shortest. Velocity-resolved RM could also isolate the putative azimuthal asymmetry that orbits around the black hole in our model. We anticipate performing velocity-resolved RM and further testing our model for RM160 in future work.

5. Summary

We have presented multiepoch optical spectroscopy of RM160, a luminous quasar that exhibits unusual broad emission-line variability in the SDSS-RM field. This object was identified from a broad search for extreme variability in quasar broad emission-line profiles and has been observed 127 times over the 9 yr monitoring period with plans to continue observations through 2026, within the SDSS-V project.

We find that RM160 exhibits normal line breathing behavior consistent with many previously studied AGNs

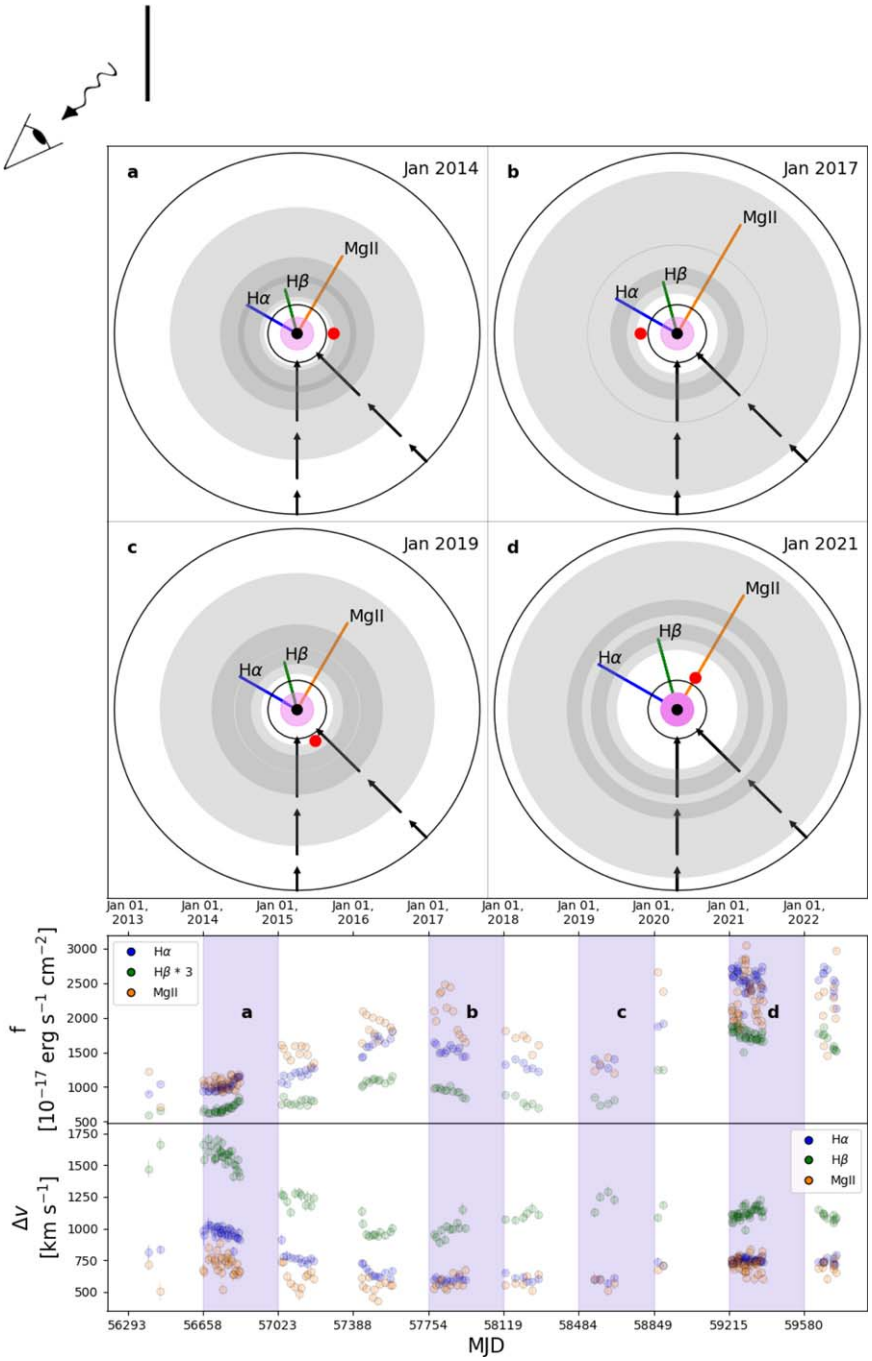

Figure 12. Our geometric and kinematic model of the BLR in RM160 (top), connected to the observed broad-line flux light curve and radial velocity shifts (bottom). The viewing angle of the observer is indicated at the top left. The radii of Hβ, Hα, and Mg II are indicated by green, blue, and orange in both the top and bottom panels, scaled to match the measured reverberation lags (Grier et al. 2017b; Homayouni et al. 2020) and with gray shading to indicate the radial extent of each emission line region. The broad-line regions "breathe," moving inward when the quasar is fainter (e.g., in 2014 and 2019) and outward when the quasar is brighter (e.g., in 2021). The red dot represents an azimuthal asymmetry in the BLR that orbits the black hole during our spectroscopic monitoring. In the animation, darker circles indicate the flux and radial velocity in the bottom panels at the same time as the model in the top panels. In the still images, the labels a, b, c, and d indicate representative time windows (also shaded purple) for the BLR model in the top panels and corresponding flux and line center in the bottom panels. A combination of radial inflow (vectors), azimuthal asymmetry (red spot), and line breathing (green, blue, and red lines and gray shading) can explain the unusual broad-line variability of RM160. The online version of this figure is an animation. The animation is 0:24 minutes long and shows the evolution of our BLR model from 2013 to 2022 (top) along with the corresponding evolution of the flux and line center, respectively, in the bottom panels.

(An animation of this figure is available.)

(e.g., Barth et al. 2015; Wang et al. 2020) in the variations of line flux and line width σ, but there is a sizable discrepancy between line width σ and FWHM for the Balmer series (Hβ and Hα). We find that the shape of the line profile (as indicated by FWHM/σ) changes over time for the Balmer series from a boxy line profile (FWHM/$\sigma > 2.355$) to a cuspy profile (FWHM/$\sigma < 2.355$) with increasing flux throughout the 9 yr monitoring period. This likely indicates asymmetry in the radial distribution of the broad-line gas, where a greater contribution from distant, low-velocity gas increases the line core and makes it appear peakier in the luminous phase.

Dramatic radial velocity variations occur in each of the three broad emission lines (Mg II, Hβ, and Hα), which all follow the same qualitative trend of starting red, shifting bluer over a few years, and then getting redder near the end of the monitoring. The radial velocity shifts are not well explained by a black hole binary because the best-fit period corresponds to the inner BLR orbits, such that a putative binary would have disrupted the BLR gas.

Our explanation for the large radial velocity shifts in the broad emission lines of RM160 is a BLR with azimuthal asymmetry and a gradient of inflow velocity in the radial direction coupled with flux-driven changes to the optimal emission region (line breathing), as illustrated in Figure 12. Similar instances of line-profile variability due to complex gas kinematics in the BLR are likely to represent an important source of false positives in radial velocity searches for binary black holes. The long-duration, wide-field, and many-epoch spectroscopic monitoring of SDSS-V/BHM-RM will be excellent for studying such systems and helping to understand the various mechanisms driving BLR dynamics.

L.B.F., J.R.T., and M.C.D. acknowledge support from NSF grant CAREER-1945546, and with C.J.G. acknowledge support from NSF grant AST-2108668. J.R.T., C.J.G., and Y. S. also acknowledge support from NSF grant AST-2009539. M.K. acknowledges support by DFG grant KR 3338/4-1. B.T. acknowledges support from the European Research Council (ERC) under the European Union's Horizon 2020 research and innovation program (grant agreement 950533) and from the Israel Science Foundation (grant 1849/19). X.L. acknowledges support from NSF grant AST-2206499. C.R. acknowledges support from the Fondecyt Iniciación grant 11190831 and ANID BASAL project FB210003. R.J.A. acknowledges support by ANID BASAL FB210003 and by FONDECYT grant number 1191124. M.L.M.-A. acknowledges financial support from Millennium Nucleus NCN19$_{058}$ (TITANs).

Funding for the Sloan Digital Sky Survey V has been provided by the Alfred P. Sloan Foundation, the Heising–Simons Foundation, the National Science Foundation, and the Participating Institutions. SDSS acknowledges support and resources from the Center for High-Performance Computing at the University of Utah. The SDSS website is www.sdss5.org.

SDSS is managed by the Astrophysical Research Consortium for the Participating Institutions of the SDSS Collaboration, including the Carnegie Institution for Science, Chilean National Time Allocation Committee (CNTAC) ratified researchers, the Gotham Participation Group, Harvard University, Heidelberg University, The Johns Hopkins University, L'Ecole polytechnique fédérale de Lausanne (EPFL), Leibniz-Institut für Astrophysik Potsdam (AIP), Max-Planck-Institut für Astronomie (MPIA Heidelberg), Max-Planck-Institut für Extraterrestrische Physik (MPE), Nanjing University, National Astronomical Observatories of China (NAOC), New Mexico State University, The Ohio State University, Pennsylvania State University, Smithsonian Astrophysical Observatory, Space Telescope Science Institute (STScI), the Stellar Astrophysics Participation Group, Universidad Nacional Autónoma de México, University of Arizona, University of Colorado Boulder, University of Illinois at Urbana-Champaign, University of Toronto, University of Utah, University of Virginia, Yale University, and Yunnan University.

Software: `AstroPy` (Astropy Collaboration et al. 2013, Astropy2018), `Matplotlib` (Hunter 2007), `NumPy` (Harris et al. 2020), `SciPy` (Virtanen et al. 2020), `linmix` (Kelly 2007), `PyQSOFit` (Guo et al. 2018; Shen et al. 2019), `specutils` (Earl et al. 2022).

Appendix
Alternative Fitting Procedures

Our paper uses a nonparametric approach to measuring the broad emission lines of RM160. In this Appendix, we fit the emission-line properties with alternative methods in order to ensure that our conclusions about the quasar's dramatic changes in line flux, width, and radial velocity are robust to the choice of fitting method. Section A.1 describes the results of single-Gaussian fits for the broad emission lines. Section A.2 instead uses `PyQSOFit` (Guo et al. 2018; Shen et al. 2019), a spectral fitting code that fits the quasar continuum, iron psuedo-continuum, and broad and narrow emission lines with multiple Gaussians. Section A.3 compares the three fitting methods and concludes that our conclusions about the quasar's dramatic broad-line breathing and radial velocity shifts are robust to different fitting methods.

A.1. Single-Gaussian Fits

The first alternative fitting method was to fit the broad emission lines with a single Gaussian. Similarly to our nonparametric measurements, we begin with the same continuum-subtracted spectra describe in Section 3.1. We then used the Gaussian1D method from the ASTROPY package (Astropy Collaboration et al. 2013, 2018) in order to fit a single Gaussian to each of the narrow and broad emission lines.

For each individual emission-line region, we followed the initial procedure in Section 3.2, in that we tied the line centers and line widths of the narrow emission lines to [O III] λ5007 and constrained the amplitude of [O III] λ4959 to be 1/3 that of [O III] λ5007. In what follows, we briefly describe the steps to obtain the broad emission-line component in each emission-line region.

For Mg II, we fit the individual spectra with a single Gaussian because there are no narrow emission lines within the Mg II emission-line region.

For Hα, we simultaneously fit the narrow lines ([N II] λ6548, narrow Hα, [N II] λ6584, [S II] λ6718, and [S II] λ6732) and the broad Hα emission line with no constraints on the amplitude of any emission line. This simultaneous fitting of all of the narrow lines and the broad Hα component produced reliable fits.

For Hβ, degeneracies between the lines made it difficult to simultaneously fit the narrow lines (narrow Hβ, [O III] λ4959, and [O III] λ5007) while also fitting the broad Hβ component reliably well. Instead, we constrained the amplitude of the narrow Hβ line to that which produced the smoothest residual in the median spectrum fit. We then applied that narrow Hβ amplitude to the fits for all epochs along with the [O III] λ4959 and [O III] λ5007 narrow lines and produced a narrow-line-subtracted spectrum. From that, we fit a single Gaussian to the continuum and narrow-line-subtracted spectra in all epochs to fit the broad Hβ component.

For all emission lines in this fitting scheme, we calculated the FWHM using the relationship between FWHM and line width (σ) for a Gaussian, namely, FWHM $= 2.355\sigma$.

Table 2
Our Parameters Used for PyQSOFit

Line	Type	n_gauss	λ_{rest}
Hα	broad	2.0	6564.61
Hα	narrow	1.0	6564.61
[N II] λ6549	narrow	1.0	6549.85
[N II] λ6585	narrow	1.0	6585.28
[S II] λ6718	narrow	1.0	6718.29
[S II] λ6732	narrow	1.0	6732.67
Hβ	broad	2.0	4862.68
Hβ	narrow	1.0	4862.68
[O III] λ4959	narrow	1.0	4960.30
[O III] λ5007	narrow	1.0	5008.24
Mg II	broad	2.0	2798.75
Mg II	narrow	1.0	2798.75

Note. The first column is the name of the emission line, the second is the type of emission line (broad or narrow), the third is the number of Gaussians used in the fit, and the fourth is the rest-frame central wavelength.

We employed bootstrap resampling to estimate the uncertainties in line flux, line center, line width (σ), and FWHM similar to our approach to estimating uncertainty in Section 3.4. We resampled each individual spectrum 200 times by sampling the fluxes within its Gaussian uncertainties in the respective epoch. We adopted the standard deviations of the 200 resampled spectra as our uncertainties for each epoch.

A.2. PyQSOFit

The second alternative fitting method was to fit the entire spectrum with the robust quasar-fitting algorithm PyQSOFit. The considerations for the continuum fit include a power law, an optical and UV Fe II template, and a fifth-order polynomial to account for possible dust reddening. PyQSOFit allows the user to select the emission-line and continuum components that are included in the overall fit as well as to select the range of fitting for the emission lines. We show our fitting parameters in Table 2.

We left most of the default parameters unchanged, except for turning off the dereddening and host decomposition since our fits within the relatively narrow wavelength regions around the broad lines will be unaffected by reddening and contributions from the host galaxy. We decided to fit the narrow emission lines with a single Gaussian, consistent with the fitting methods in Section 3.4 and Appendix A.1. We allowed two Gaussians to fit the broad lines in order to better capture the complex shapes of the line profiles.

PyQSOFit was used to obtain the flux, line width (σ), FWHM, and line center of the Mg II, Hβ, and Hα emission

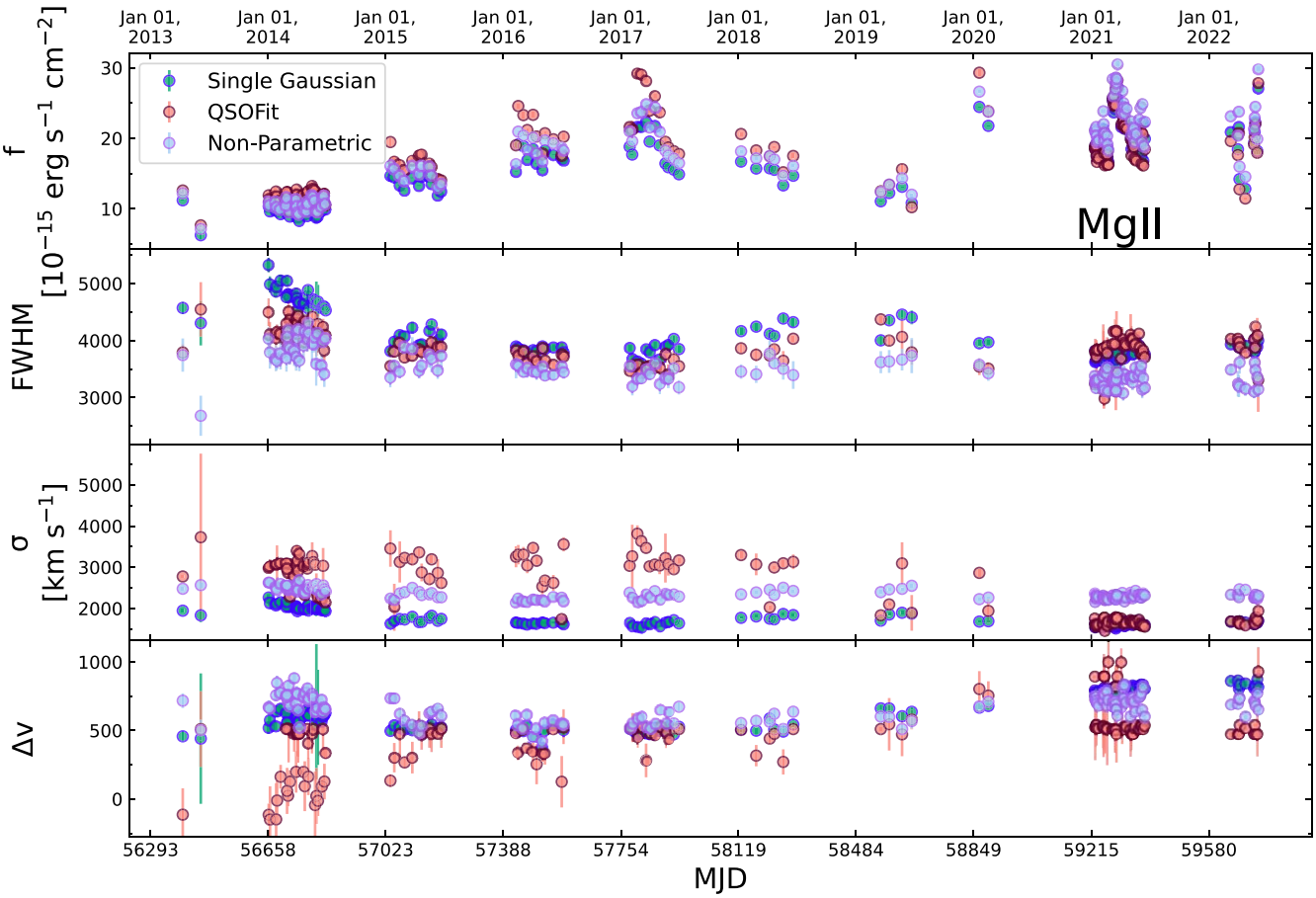

Figure 13. Variability of the Mg II broad emission-line profile, as quantified by our three fitting methods for the line flux (top row), FWHM (second row), line width σ (third row), and the line-center velocity shifts Δv (bottom row). The FWHM, line width σ, and line-center velocity shift Δv are all in units of km s^{-1}. The measured flux and FWHM are consistent across all methods. There are differences in the measured σ and Δv due to differences in fitting the wings of the line profile, but all three methods find similar qualitative trends of line breathing and shifts in the line center.

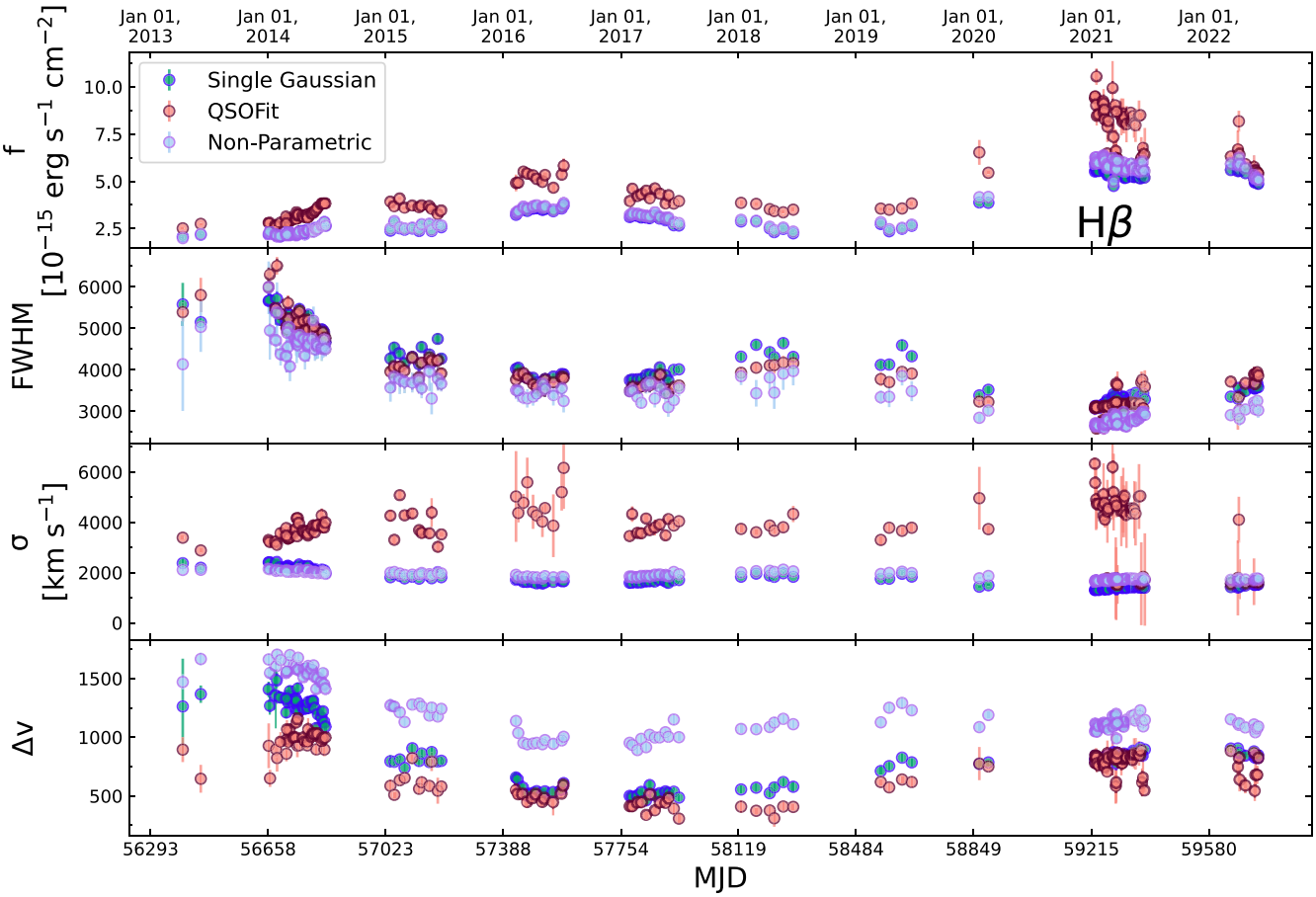

Figure 14. Variability of the Hβ broad emission-line profile, as quantified by the three fitting methods for the line flux (top row), FWHM (second row), line width σ (third row), and the line-center velocity shifts Δv (bottom row). The FWHM, line width σ, and line-center velocity shift Δv are all in units of km s^{-1}. The Hβ line has a complex profile (see Figure 2) and the three methods result in different line fluxes, σ widths, and line centers due to including different amounts of the line wings in the fit. Despite these differences, all three methods find similar qualitative trends for the variability of the line.

lines for each epoch. We use the uncertainties reported by `PyQSOFit` for each of the fitted quantities.

Note that our `PyQSOFit` analysis is not exactly analogous to Wang et al. (2020) because they used three Gaussians to fit each broad emission line. Furthermore, they rejected epochs that are 2σ below the mean S/N for each season. Wang et al. (2020) also use a window of $[-2.5 \times \mathrm{MAD},\ 2.5 \times \mathrm{MAD}]$ to compute σ_{line} so as to eliminate the effects of noise and blending in the line wings.

A.3. Comparison of the Three Fitting Methods.

Figures 13, 14, and 15 show the variability of the Mg II, Hβ, and Hα broad emission-line profiles as quantified by the three different fitting methods.

The three methods result in very similar flux light curves for the Hα and Mg II lines. The different methods also find very similar FWHM measurements for the three lines, implying that the FWHM measurement is robust to the details of the emission-line models (Dalla Bontà et al. 2020). On the other hand, the three methods have large differences in the σ measurement. The σ line width is highly sensitive to the wings of the line and so is susceptible to small differences in the fitted line profile. Among the three lines, Hβ has the largest differences in measured quantities between the three lines, owing to its complex and asymmetric line profile (shown in Figure 2), which is highly sensitive to small differences in fitting.

Despite differences in the details of the line fits, the three methods result in similar *qualitative* trends for all three emission lines. That is, the differences between methods are generally systematic offsets: e.g., `QSOFit` measures broader σ and lower Δv for all lines, as well as brighter Hβ, than the other methods. The similar overall qualitative trends mean that our general conclusions about the relative changes in the line profiles are not dependent on the details of the fitting method.

Figure 16 shows the line breathing behavior measured by the three fitting methods. We fit the relationships in each panel using the Bayesian linear regression package `linmix` (Kelly 2007). The slopes are shown at the bottom left of each panel where β_{QF} corresponds to the slope for the QSOFit fitting method, β_{SG} corresponds to the slope for the single-Gaussian fitting method, and β_{NP} corresponds to the slope for our nonparametric measurements. The slopes for FWHM are broadly similar for all three fits to each emission line, while the slopes for line width σ show large differences. As noted above in the discussion of Figures 13, 14, and 15, measurements of line width σ are more sensitive to the details of the

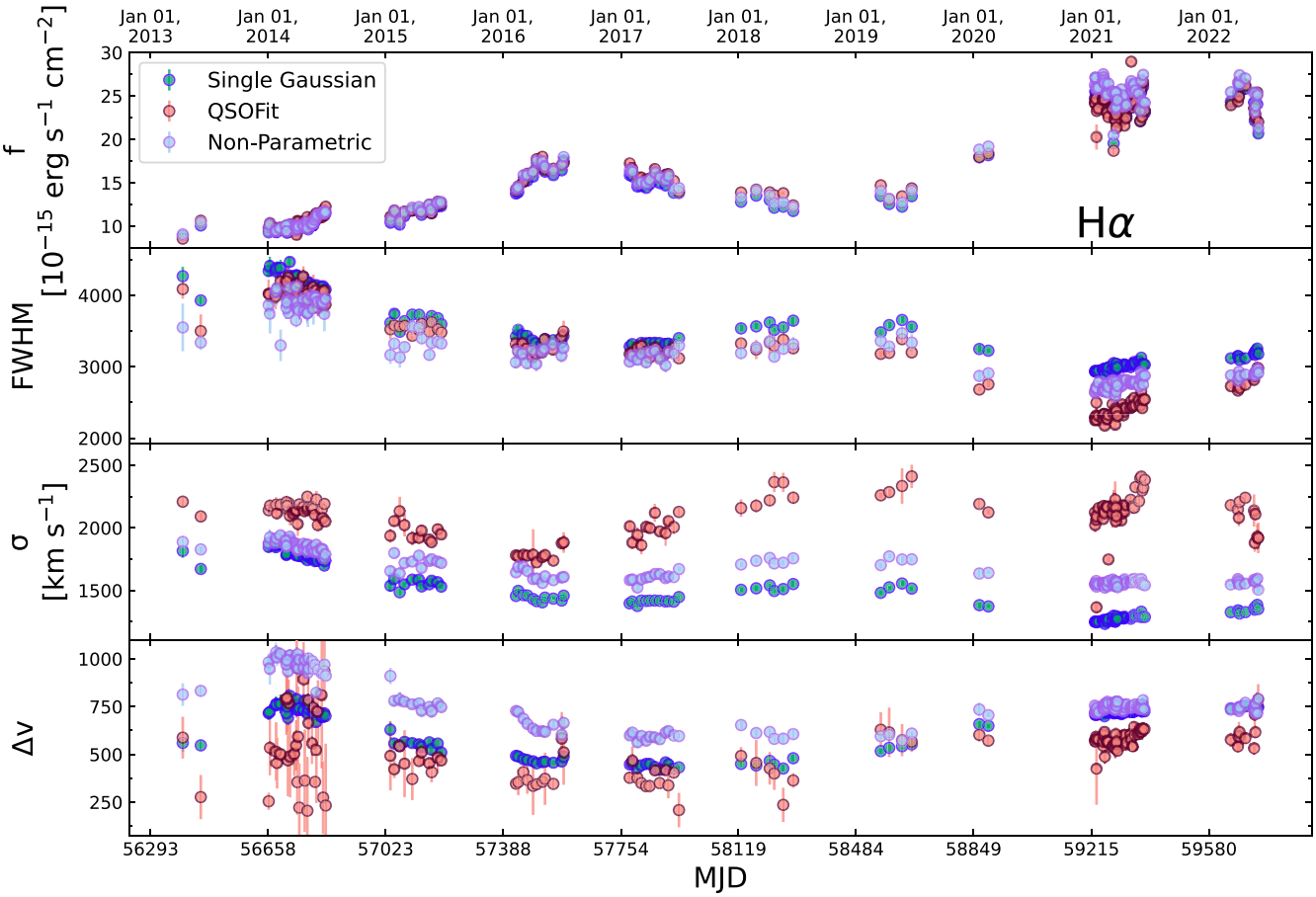

Figure 15. Variability of the Hα broad emission-line profile, as quantified by our three fitting methods for the line flux (top row), FWHM (second row), line width σ (third row), and the line-center velocity shifts Δv (bottom row). The FWHM, line width σ, and line-center velocity shift Δv are all all in units of km s^{-1}. As for the fit to Mg II, the measured flux and FWHM are consistent across all methods. There are differences in the measured σ and Δv due to differences in fitting the wings of the line profile, but all three methods find similar qualitative trends of line breathing and shifts in the line center.

line profile and so are more dependent on the differences in best-fit models from each method. From this investigation we note that characterizing quasar line breathing with σ is likely to depend significantly on the details of the fitting method, especially for emission lines that change shape such as in RM160 (see Figure 10). Measurements of FWHM line width, on the other hand, are less sensitive to details of the model fitting.

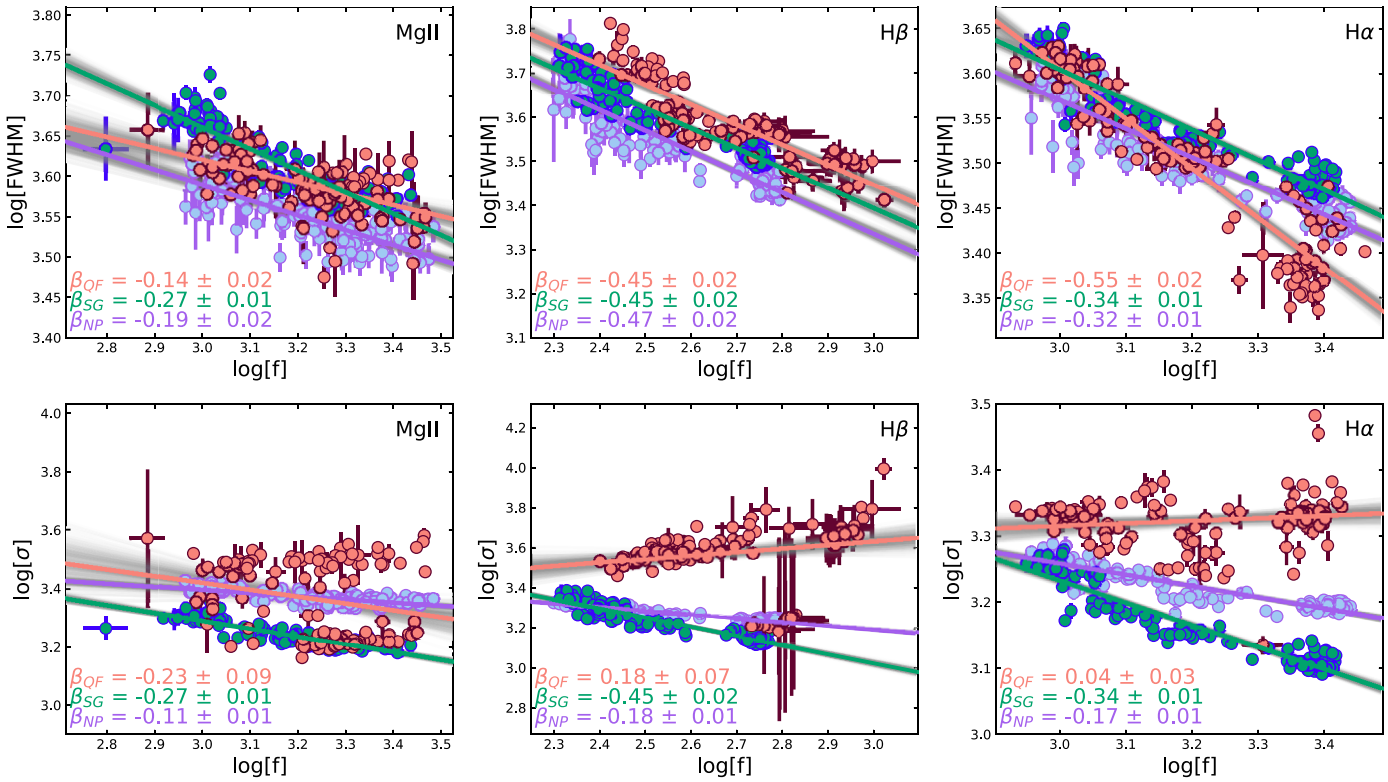

Figure 16. Plots of line width vs. line flux for RM160 for all fitting methods. The purple points are from the nonparametric fitting method, the pink points are from QSOFit, and the green points are from the single-Gaussian fitting method. The colors of the lines of best fit correspond to the colors of the data points. The top panels show the FWHM vs. line flux for Mg II, Hβ, and Hα (left to right). The bottom panels show the line width σ vs. line flux for Mg II, Hβ, and Hα (left to right). The individual slopes are shown at the bottom left of each panel, where $\beta_{\rm QF}$ is the slope for the QSOFit fitting method, $\beta_{\rm SG}$ is the slope for the single-Gaussian fitting method, and $\beta_{\rm NP}$ is the slope for our nonparametric measurements. The best-fit slopes for FWHM are broadly consistent, while we see large discrepancies between the slopes for line width σ. This seems consistent with what we see for the values of FWHM and line width σ in Figures 13, 14, and 15, where we see a general consensus for FWHM values across all schemes, and differences in values of line width σ.

ORCID iDs

Logan B. Fries https://orcid.org/0000-0001-8032-2971
Jonathan R. Trump https://orcid.org/0000-0002-1410-0470
Megan C. Davis https://orcid.org/0000-0001-9776-9227
C. J. Grier https://orcid.org/0000-0001-9920-6057
Yue Shen https://orcid.org/0000-0003-1659-7035
Scott F. Anderson https://orcid.org/0000-0002-6404-9562
Tom Dwelly https://orcid.org/0000-0002-4459-9233
Michael Eracleous https://orcid.org/0000-0002-3719-940X
Y. Homayouni https://orcid.org/0000-0002-0957-7151
Keith Horne https://orcid.org/0000-0003-1728-0304
Sean Morrison https://orcid.org/0000-0002-6770-2627
Jessie C. Runnoe https://orcid.org/0000-0001-8557-2822
Benny Trakhtenbrot https://orcid.org/0000-0002-3683-7297
Roberto J. Assef https://orcid.org/0000-0002-9508-3667
W. N. Brandt https://orcid.org/0000-0002-0167-2453
Joel Brownstein https://orcid.org/0000-0002-8725-1069
Collin Dabbieri https://orcid.org/0000-0001-7306-1830
Alexander Fix https://orcid.org/0000-0003-4444-0115
Gloria Fonseca Alvarez https://orcid.org/0000-0003-0042-6936
Sara Frederick https://orcid.org/0000-0001-9676-730X
P. B. Hall https://orcid.org/0000-0002-1763-5825
Anton M. Koekemoer https://orcid.org/0000-0002-6610-2048
Jennifer I-Hsiu Li https://orcid.org/0000-0002-0311-2812
Xin Liu https://orcid.org/0000-0003-0049-5210
Mary Loli Martínez-Aldama https://orcid.org/0000-0002-7843-7689
Claudio Ricci https://orcid.org/0000-0001-5231-2645
Donald P. Schneider https://orcid.org/0000-0001-7240-7449
Hugh W. Sharp https://orcid.org/0000-0001-9616-1789
Matthew J. Temple https://orcid.org/0000-0001-8433-550X
Qian Yang https://orcid.org/0000-0002-6893-3742
Grisha Zeltyn https://orcid.org/0000-0002-7817-0099
Dmitry Bizyaev https://orcid.org/0000-0002-3601-133X

References

Ackermann, M., Ajello, M., Albert, A., et al. 2015, ApJL, 813, L41
Almeida, A., Anderson, S. F., Argudo-Fernández, M., et al. 2023, arXiv:2301.07688
Astropy Collaboration, Price-Whelan, A. M., Sipőcz, B. M., et al. 2018, AJ, 156, 123
Astropy Collaboration, Robitaille, T. P., Tollerud, E. J., et al. 2013, A&A, 558, A33
Ayubinia, A., Xue, Y., Woo, J.-H., et al. 2022, Univ, 8, 559
Barth, A. J., Bennert, V. N., Canalizo, G., et al. 2015, ApJS, 217, 26
Barth, A. J., Nguyen, M. L., Malkan, M. A., et al. 2011a, ApJ, 732, 121
Barth, A. J., Pancoast, A., Thorman, S. J., et al. 2011b, ApJL, 743, L4
Bentz, M. C., Denney, K. D., Grier, C. J., et al. 2013, ApJ, 767, 149
Bentz, M. C., Horne, K., Barth, A. J., et al. 2010a, ApJL, 720, L46
Bentz, M. C., Walsh, J. L., Barth, A. J., et al. 2009, ApJ, 705, 199
Bentz, M. C., Walsh, J. L., Barth, A. J., et al. 2010b, ApJ, 716, 993
Bentz, M. C., Williams, P. R., Street, R., et al. 2021, ApJ, 920, 112
Blandford, R. D., & McKee, C. F. 1982, ApJ, 255, 419
Blanton, M. R., Bershady, M. A., Abolfathi, B., et al. 2017, AJ, 154, 28
Bolton, A. S., Schlegel, D. J., & Aubourg, É. 2012, AJ, 144, 144

Brotherton, M. S., Wills, B. J., Steidel, C. C., & Sargent, W. L. W. 1994, ApJ, 423, 131
Cackett, E. M., Bentz, M. C., & Kara, E. 2021, iSci, 24, 102557
Cackett, E. M., & Horne, K. 2006, MNRAS, 365, 1180
Charisi, M., Bartos, I., Haiman, Z., et al. 2016, MNRAS, 463, 2145
Chen, Y.-C., Liu, X., Liao, W.-T., et al. 2020, MNRAS, 499, 2245
Clavel, J., Reichert, G. A., Alloin, D., et al. 1991, ApJ, 366, 64
Dalla Bontà, E., Peterson, B. M., Bentz, M. C., et al. 2020, ApJ, 903, 112
Denney, K. D., Watson, L. C., Peterson, B. M., et al. 2009, ApJ, 702, 1353
Dexter, J., Xin, S., Shen, Y., et al. 2019, ApJ, 885, 44
Earl, N., Tollerud, E., Jones, C., et al. 2022, astropy/specutils: V1.7.0, vv1.7.0, Zenodo, doi:10.5281/zenodo.6207491
Eisenstein, D. J., Weinberg, D. H., Agol, E., et al. 2011, AJ, 142, 72
Eracleous, M., Boroson, T. A., Halpern, J. P., & Liu, J. 2012, ApJS, 201, 23
Ferland, G. J., Peterson, B. M., Horne, K., Welsh, W. F., & Nahar, S. N. 1992, ApJ, 387, 95
Foltz, C. B., Peterson, B. M., Capriotti, E. R., et al. 1981, ApJ, 250, 508
Gaskell, C. M. 1983, in Quasars and Gravitational Lenses; Proc. of the Twenty-fourth Liege International Astrophysical Colloquium, ed. J.-P. Swings, 473
Gezari, S. 2021, ARA&A, 59, 21
Goad, M. R., & Korista, K. T. 2014, MNRAS, 444, 43
Graham, M. J., Djorgovski, S. G., Stern, D., et al. 2015, Natur, 518, 74
Gravity Collaboration, Amorim, Bauböck, A., et al. 2020, A&A, 643, A154
Grier, C. J., Martini, P., Watson, L. C., et al. 2013, ApJ, 773, 90
Grier, C. J., Pancoast, A., Barth, A. J., et al. 2017a, ApJ, 849, 146
Grier, C. J., Peterson, B. M., Horne, K., et al. 2013, ApJ, 764, 47
Grier, C. J., Trump, J. R., Shen, Y., et al. 2017b, ApJ, 851, 21
Gunn, J. E., Siegmund, W. A., Mannery, E. J., et al. 2006, AJ, 131, 2332
Guo, H., Liu, X., Shen, Y., et al. 2019, MNRAS, 482, 3288
Guo, H., Shen, Y., & Wang, S. 2018, PyQSOFit: Python code to fit the spectrum of quasars, Astrophysics Source Code Library, ascl:1809.008
Harris, C. R., Millman, K. J., van der Walt, S. J., et al. 2020, Natur, 585, 357
Herrmann, F., Hinder, I., Shoemaker, D., Laguna, P., & Matzner, R. A. 2007, ApJ, 661, 430
Homan, D., MacLeod, C. L., Lawrence, A., Ross, N. P., & Bruce, A. 2020, MNRAS, 496, 309
Homayouni, Y., Trump, J. R., Grier, C. J., et al. 2020, ApJ, 901, 55
Hunter, J. D. 2007, CSE, 9, 90
Kelly, B. C. 2007, ApJ, 665, 1489
Kelly, B. C., Bechtold, J., & Siemiginowska, A. 2009, ApJ, 698, 895
King, A. 2016, MNRAS, 456, L109
Kollmeier, J. A., Zasowski, G., Rix, H.-W., et al. 2017, arXiv:1711.03234
Korista, K. T., & Goad, M. R. 2004, ApJ, 606, 749
Kovačević-Dojčinović, J., Dojčinović, I., Lakićević, M., & Popović, L. 2022, A&A, 659, A130
Li, J. I.-H., Shen, Y., Ho, L. C., et al. 2023, arXiv:2301.04177
Li, S.-S., Feng, H.-C., Liu, H. T., et al. 2022, ApJ, 936, 75
Li, Y.-R., Wang, J.-M., Ho, L. C., et al. 2016, ApJ, 822, 4
Li, Y.-R., Wang, J.-M., Zhang, Z.-X., et al. 2019, ApJS, 241, 33
Liao, W.-T., Chen, Y.-C., Liu, X., et al. 2021, MNRAS, 500, 4025
Liu, X., Shen, Y., Bian, F., Loeb, A., & Tremaine, S. 2014, ApJ, 789, 140
Loeb, A. 2010, PhRvD, 81, 047503
Lynden-Bell, D. 1969, Natur, 223, 690
MacLeod, C. L., Ivezić, Ž., Kochanek, C. S., et al. 2010, ApJ, 721, 1014
Molina, J., Ho, L. C., Wang, R., et al. 2022, ApJ, 935, 72
Netzer, H. 1975, MNRAS, 171, 395
Newville, M., Stensitzki, T., Allen, D. B., & Ingargiola, A. 2014, LMFIT: Non-Linear Least-Square Minimization and Curve-Fitting for Python, v0.8.0, Zenodo, doi:10.5281/zenodo.11813
Pancoast, A., Brewer, B. J., & Treu, T. 2014, MNRAS, 445, 3055
Park, D., Woo, J.-H., Treu, T., et al. 2012, ApJ, 747, 30
Peterson, B. M. 1993, PASP, 105, 247
Peterson, B. M., Denney, K. D., De Rosa, G., et al. 2013, ApJ, 779, 109
Peterson, B. M., Foltz, C. B., Byard, P. L., & Wagner, R. M. 1982, ApJS, 49, 469
Rakshit, S., & Woo, J.-H. 2018, ApJ, 865, 5
Rees, M. J., Netzer, H., & Ferland, G. J. 1989, ApJ, 347, 640
Reichert, G. A., Rodriguez-Pascual, P. M., Alloin, D., et al. 1994, ApJ, 425, 582
Rojas, A. F., Sani, E., Gavignaud, I., et al. 2020, MNRAS, 491, 5867
Runnoe, J. C., Eracleous, M., Pennell, A., et al. 2017, MNRAS, 468, 1683
Sandrinelli, A., Covino, S., Treves, A., et al. 2018, A&A, 615, A118
Sergeev, S. G., Doroshenko, V. T., Dzyuba, S. A., et al. 2007, ApJ, 668, 708
Severgnini, P., Cicone, C., Della Ceca, R., et al. 2018, MNRAS, 479, 3804
Seyfert, C. K. 1943, ApJ, 97, 28
Shapovalova, A. I. 2010, A&A, 509, A106
Shen, Y., Brandt, W. N., Dawson, K. S., et al. 2015, ApJS, 216, 4
Shen, Y., Hall, P. B., Horne, K., et al. 2019, ApJS, 241, 34
Shen, Y., Liu, X., Loeb, A., & Tremaine, S. 2013, ApJ, 775, 49
Smee, S. A., Gunn, J. E., Uomoto, A., et al. 2013, AJ, 146, 32
Storchi-Bergmann, T. 2010, in IAU Symp. 267, Co-Evolution of Central Black Holes and Galaxies, ed. B. M. Peterson et al. (Cambridge: Cambridge Univ. Press), 290
Storey, P. J., & Zeippen, C. J. 2000, MNRAS, 312, 813
Sturm, E., Dexter, J., Pfuhl, O., et al. 2018, Natur, 563, 657
Tremaine, S., Shen, Y., Liu, X., & Loeb, A. 2014, ApJ, 794, 49
U, U. V., Barth, A. J., & Vogler, H. A. 2022, ApJ, 925, 52
Ulrich, M.-H., Maraschi, L., & Urry, C. M. 1997, ARA&A, 35, 445
Valtonen, M. J., Lehto, H. J., Nilsson, K., et al. 2008, Natur, 452, 851
Vanden Berk, D. E., Richards, G. T., Bauer, A., et al. 2001, AJ, 122, 549
Vanden Berk, D. E., Wilhite, B. C., Kron, R. G., et al. 2004, ApJ, 601, 692
Vaughan, S., Uttley, P., Markowitz, A. G., et al. 2016, MNRAS, 461, 3145
Villafaña, L., Williams, P. R., Treu, T., et al. 2022, ApJ, 930, 52
Virtanen, P., Gommers, R., Oliphant, T. E., et al. 2020, NatMe, 17, 261
Wang, S., Shen, Y., Jiang, L., et al. 2020, ApJ, 903, 51
Wilhite, B. C., Berk, D. E. V., Brunner, R. J., & Brinkmann, J. V. 2006, ApJ, 641, 78
Woo, J.-H., Yoon, Y., Park, S., Park, D., & Kim, S. C. 2015, ApJ, 801, 38
Yang, Q., Shen, Y., Chen, Y.-C., et al. 2020, MNRAS, 493, 5773
York, D. G., Adelman, J., Anderson, J. E. J., et al. 2000, AJ, 120, 1579
Yu, Q. 2002, MNRAS, 331, 935
Zhang, X. 2022, MNRAS, 512, 1003